

# Enhanced Geological Prediction for Tunnel Excavation Using Full Waveform Inversion Integrating Sobolev Space Regularization with a Quadratic Penalty Method

**Jiahang Li <sup>a,\*</sup>, Junichi Takekawa <sup>a</sup>, Keisuke Kurihara <sup>b</sup>, Karnallisa Desmy Halim <sup>b</sup>, Masumoto Kazuhiko <sup>b</sup>, Miyajima Yasuyuki <sup>b</sup>**

*<sup>a</sup>Department of Civil and Earth Resources Engineering, Graduate School of Engineering, Kyoto University, Kyoto 615-8246, Japan*

*<sup>b</sup>Kajima Technical Research Institute, Kajima Corporation, Tokyo 182-0036, Japan*

*\*Corresponding Author: Jiahang Li*

*Department of Civil and Earth Resources Engineering, Kyoto University, Kyoto 615-8246, Japan.*

*Email address: [li.jiahang.n83@kyoto-u.ac.jp](mailto:li.jiahang.n83@kyoto-u.ac.jp)*

**Running head: FWI for Tunnel Excavation Prediction**

*Date: June, 6, 2024*

**Keywords:** Full Waveform Inversion, Tunnel Advance Prediction, Quadratic Penalty Method, Regularization, Noise

## **ABSTRACT**

In the process of tunnel excavation, advance geological prediction technology has become indispensable for safe, economical, and efficient tunnel construction. Although traditional methods such as drilling and geological analysis are effective, they typically involve destructive processes, carry high risks, and incur significant costs. In contrast, non-destructive geophysical exploration offers a more convenient and economical alternative. However, the accuracy and precision of these non-destructive methods can be severely compromised by complex geological structures and environmental noise. To address these challenges effectively, a novel approach using frequency domain full waveform inversion, based on a penalty method and Sobolev space regularization, has been proposed to enhance the performance of non-destructive predictions. The proposed method constructs a soft-constrained optimization problem by restructuring the misfit function into a combination of data misfit and wave equation drive terms to enhance convexity. Additionally, it semi-extends the search space to both the wavefield and the model parameters to mitigate the strong nonlinearity of the optimization, facilitating high-resolution inversion. Furthermore, a Sobolev space regularization algorithm is introduced to flexibly adjust the regularization path, addressing issues related to noise and artefacts to enhance the robustness of the algorithm. We evaluated the modified full waveform inversion with several tunnel fault models by comparing the results of the enhanced method with those of traditional least squares-based Tikhonov regularization and total variation regularization full waveform inversion methods. The verification results confirm the superior capabilities of the proposed method as expected.

## 1. Introduction

The construction of underground infrastructures has become increasingly comprehensive and influential due to population growth and urbanization. Nearly all underground construction projects involve constructing tunnels, so it's crucial to enhance the safety and reliability of tunnel construction processes (Li et al., [2017](#)). During underground excavation, particularly in tunnel excavation, the presence of potential hazards such as fractured zones, faults, and aquifers ahead of the tunnel poses significant safety risks (Zhang et al., [2018](#)). Therefore, before and during construction, geophysical exploration and measurements of the geological conditions and underground structures at the site are necessary to provide general geological information about the tunnel area. Hence, employing a non-destructive tunnel advance exploration technique to predict unidentified geological structures ahead of the tunnel is of paramount importance (Xu et al., [2021](#)).

Geophysical exploration is a primary method for detecting and identifying underground geological structures. In seismic exploration ahead of the tunnel face, the seismic source emits non-destructive waves into the ground. The propagating seismic waves generate reflected and refracted waves and are picked up by receivers, helping to estimate relevant underground geological information (Wai-Lok Lai et al., [2018](#)). Currently available advance seismic geological prediction methods include tunnel seismic prediction (TSP), true reflection tomography (TRT), horizontal seismic profiling (HSP), tunnel seismic tomography (TST), tunnel seismic while drilling (TSWD), and tunnel geology prediction (TGP) (Hanson et al., [2002](#); Petronio et al., [2007](#); Cheng et al., [2014](#); Yu et al., [2022](#)). In the late 1970s, engineers in Germany and England first explored geological structures ahead of tunnel faces using the air seismic phase. In the 1990s, the Swiss Surveying Technology Co., Ltd. developed an advance TSP system. Subsequently, in the 1990s, the TRT technology was developed by a US company. In the late 1990s, a new method of vertical seismic profiling for tunnels (HSP) emerged and was widely applied (Inazaki et al., [1999](#)). Ashida (2002) proposed to use of three-component seismic records to enhance the imaging capability by incorporating the incident directions of seismic waves. However, these methods are constrained and limited because the observation systems are confined to tunnel environments. This leads to

incomplete seismic data collection that fails to meet the requirements for high-precision imaging (Yu et al., [2022](#)). Further, these methods share the same limitations as conventional seismic exploration methods; they do not utilize all seismic wave information, which could lead to the potential neglect of critical seismic information during the process of separating multiple waves.

A noteworthy method in the realm of geophysical exploration is full waveform inversion (FWI), a procedure that surpasses the Born approximation, first proposed by Tarantola (Tarantola, [1984](#)). The core theory is to forward the model based on the received seismic data. This involves comparing it with the wavefield of the initial model using least squares (LS). Then, optimization algorithms subsequently determine the update direction to achieve the minimum value and obtain an inversion model close to the true model after a finite number of iterations. FWI, due to its computation of the entire wavefield information, has long been highly anticipated compared to other conventional algorithms (Virieux and Operto, [2009](#)). While the algorithm was proposed earlier, the high computational requirement for forward modelling restrains its widespread industrial utilization in the early 21st century, remaining primarily in the early stages of research (Tromp, [2020](#)). However, with the release of large-scale computational resources and reduced computational burden today, applying FWI in the industrial sector has become feasible. Over the several past decades, FWI has seen tremendous momentum in the oil and gas industry, with new computing processes evolving from conventional LS and becoming an irreplaceable mainstream oil and gas exploration technology supported by various optimization algorithms (Sun et al., [2015](#)). However, there has been limited research and application examples of FWI in mechanized tunnel excavation, particularly in tunnel advance prediction. There remains extensive research space and application prospects for utilizing FWI to predict tunnel excavation processes in advance (Trapp and Nestorović, [2022](#)).

There are several factors constraining the widespread application of FWI in engineering problems. Firstly, the nonlinear nature of single-parameter acoustic FWI poses challenges, leading to optimization processes getting trapped in local minima and consequently reducing the precision of the inversion (Biondi et al., [2021](#)). Additionally, the phenomenon of cycle-skipping resulting from the absence of low-frequency information exacerbates this issue, rendering FWI overly reliant on low

frequencies or initial models (Métivier et al., [2016](#)). To address these challenges, some engineering extensions to FWI are proposed. Musayev et al. (2016) first applied frequency-domain FWI to tunnel detection in 2016 and discussed its feasibility in imaging velocity fields. Nguyen and Nestorovic (2018) proposed an enhanced tunnel seismic wave FWI method to locate anomalous areas ahead of the tunnel face. Additionally, Bharadwaj et al. (2017) introduced an FWI approach combining the adjoint gradient method with a two-dimensional model, focusing on horizontally polarized shear waves. Furthermore, for tunnel advance prediction, Riedel et al. (2021) and Riedel et al. (2023) introduced time-domain and frequency-domain elastic wave FWI methods.

In response to the unique challenges of tunnel advance prediction, and considering that FWI is recognized as a nonlinear, non-convex inversion problem, an advanced regularization technique and an enhanced optimization algorithm are recommended during the optimization to mitigate nonlinearity and avoid entrapment in local minima. Specifically, considering the spatial constraints within the tunnel, we first deploy an external acquisition system placed outside the tunnel, with a large number of receivers positioned on the free surface or non-free surface of the overlying rock mass. In terms of algorithm, to mitigate the nonlinearity and constraints in solving the FWI problem, we introduce a quadratic penalty method into tunnel advance prediction FWI, replacing the conventional LS optimization process to enhance inversion resolution. Additionally, we suggest using a Sobolev space regularization algorithm to embed a regularization term in the misfit function, enhancing the noise resistance and artefact suppression capability of tunnel advance prediction FWI. This paper compares and discusses the multi-scale frequency-domain FWI algorithm with quadratic penalty Sobolev space regularization algorithm to LS-based other regularization algorithms including Tikhonov and total variation (TV) regularization, analyzing the influence of different adjoint-state variable, wavefields and misfits used in the proposed method on the inversion results. Lastly, the effectiveness and superiority of the enhanced algorithm are verified through the tunnel models with fault.

## **2. Methodology**

In FWI, a reasonable forward calculation is crucial for inversion, as accurate inversion is based on correct forward modelling (Virieux and Operto, [2009](#)). In geophysical exploration techniques, frequency domain FWI has attracted widespread interest and research for the exceptional accuracy and flexibility it offers, which are not constrained by overly idealized sampling rates in time (Takekawa and Mikada, [2018](#)).

### 2.1. Source-receiver frequency domain modelling

A critical component of the forward method in the frequency domain is solving the Helmholtz equation (Huang et al., [2017](#)). Helmholtz equation gives an important maths structure to comprehend geophysical phenomena. In geophysical problems, the following equation applies to the frequency-domain wave equation, particularly when considering complex media and source configurations:

$$(\Delta + \omega^2 \mathbf{m})\mathbf{u} = -L(\omega)\delta(\mathbf{x} - \mathbf{x}_s)\delta(\mathbf{z} - \mathbf{z}_s), \quad (1)$$

where  $\Delta$  is the Laplacian operator,  $\omega$  denotes the angular frequency,  $\mathbf{m}$  represents the squared slowness,  $\mathbf{u}$  denotes the wavefield,  $L(\omega)$  denotes a frequency-dependent linear operator,  $\delta(\mathbf{x} - \mathbf{x}_s)$  and  $\delta(\mathbf{z} - \mathbf{z}_s)$  denote the source at points  $\mathbf{x}_s$  and  $\mathbf{z}_s$  (Habashy et al., [2011](#)). Frequency domain FWI minimizes the LS difference between observed and computed data in the data space, iteratively updating the model based on gradient direction and model increments, which means the whole process heavily relies on the accuracy of the forward modelling. The frequency domain method, noted for its high precision in handling low-frequency components and its ability to avoid local minima, excels compared to the time domain (Ovcharenko et al., [2019](#)). These advantages make frequency domain FWI particularly beneficial for advance prediction in tunnel excavation.

## 2.2. A soft-constrained optimization

The inversion problem of the frequency FWI can be formulated as a nonlinear partial differential equation (PDE)-constrained optimization problem (Brossier et al., 2009):

$$\min_{\mathbf{m}, \mathbf{u}} \|\mathbf{P}\mathbf{u} - \mathbf{D}\|_2^2, \text{ s.t. } \mathbf{A}(\mathbf{m})\mathbf{u} = \mathbf{S}, \quad (2)$$

where the  $\mathbf{P}$  denotes observation operator,  $\mathbf{D}$  is observed data; the right side is subject to a constraint function, where  $\mathbf{A}(\mathbf{m})$  is discretized PDE,  $\mathbf{S}$  denotes the source term and  $\|\cdot\|$  represents the Euclidean norm (Aghamiry et al., 2019):

$$\mathbf{A}(\mathbf{m})\mathbf{u} = \omega^2 \text{diag}(\mathbf{m}) + \Delta, \quad (3)$$

where  $\text{diag}(\cdot)$  is the diagonalisation operation. For nonlinear constrained optimization problems, specifically Eq. (2), the Lagrange multiplier method can be used for solving by Lagrange relaxation (Gholami et al., 2022). However, solving the Eq. (2) problem requires the use of a full-space approach to jointly update three distinct variables, which are wavefield, model parameter and Lagrange multiplier, meaning that even in single-parameter acoustic inversion, it is necessary to solve a large-scale Karush–Kuhn–Tucker (KKT) conditions (Qi and Jiang, 1997). In this context, the matrix operator is a multivariate Hessian matrix, which implies a substantial computational demand (Aghazade et al., 2022). An alternative simplification involves projecting the full space onto the parameter search space, which entails computing the solution to the wave equation within the misfit to enhance computational efficiency. Based on this, the constrained optimization problem of Eq. (2) can thus be transformed into the following unconstrained optimization problem:

$$\min_{\mathbf{m}} F(\mathbf{m}) = \min_{\mathbf{m}} \|\mathbf{P}\mathbf{A}^{-1}(\mathbf{m})\mathbf{S} - \mathbf{D}\|_2^2, \quad (4)$$

the simplified unconstrained form of the misfit function  $F(\mathbf{m})$ , as expressed above, offers easier manageability compared to full-space computations. However, the inversion challenge intensifies because the PDE inverse operator  $\mathbf{A}^{-1}$  exhibits a highly oscillatory nature, which highlights the

optimization problem's inherent nonlinearity (Gholami and Aghazade, [2024](#)). Consequently, the inversion process of FWI becomes increasingly reliant on an accurate initial model or the incorporation of low-frequency information to avoid falling into local minima.

To overcome the above problems, a soft-constrained quadratic penalty term method concerning the wavefield and model parameters is proposed (Leeuwen and Herrmann, [2015](#)):

$$\min_{\mathbf{m}, \mathbf{u}} F(\mathbf{m}) = \min_{\mathbf{m}, \mathbf{u}} \|\mathbf{P}\mathbf{u} - \mathbf{D}\|_2^2 + \tau \|\mathbf{A}(\mathbf{m})\mathbf{u} - \mathbf{S}\|_2^2, \quad (5)$$

where  $\tau$  is a non-negative penalty parameter includes a scaling factor  $\gamma$ . Relative to conventional least-square algorithms, this method broadens the search space from not only the model parameter but include the wave equation. Moreover, unlike full-space constrained optimization, Eq. (4) projects the full space - encompassing the wavefield, model parameters, and the Laplacian operator onto a reduced space comprising only the wavefield and model parameters. The projection significantly alleviates the nonlinearity inherent in the inversion problem (Li et al., [2024a](#)). The closed-form expression of the wavefield of Eq. (5) by the alternating direction method is as follows:

$$\mathbf{u}^{n+1} = (\tau \mathbf{A}^T(\mathbf{m}^n) \mathbf{A}(\mathbf{m}^n) + \mathbf{P}^T \mathbf{P})^{-1} (\tau \mathbf{A}^T(\mathbf{m}^n) \mathbf{S} + \mathbf{P} \mathbf{D}), \quad (6)$$

Eq. (6) involves an alternating direction optimization strategy, where the wavefield variable is held fixed while the model parameters are updated, and  $\tau \mathbf{A}^T \mathbf{A} + \mathbf{P}^T \mathbf{P}$  involves a simplified version of the original PDE, importantly, the actual measurements are used as constraints to assist in adjusting, validating and improving the model (Leeuwen and Herrmann, [2015](#)). Optimization process using a Gauss-Newton iteration to update the model parameters and calculate the gradient concerning them to determine the direction of the next iteration. At this point, it is crucial that the adjoint state  $\mathbf{v}$  is completed synchronously with the forward and does not require an additional solution to the PDE:

$$\mathbf{v}^{n+1} = \tau (\mathbf{A}(\mathbf{m}^n) \mathbf{u}^{n+1} - \mathbf{S}), \quad (7)$$

where  $\mathbf{v}$  is the adjoint-state variable (van Leeuwen and Herrmann, [2013](#)).

Another important concept is the choice of parameters for the penalty term, how to find the



appropriate Lagrangian stability point by adjusting the penalty parameter is crucial, the specific derivation process is in Appendix A. We need to find a part of the penalty parameter based on the real part of the largest eigenvalue matrix:

$$\eta = \Re(\Lambda_{\max}(\mathbf{A}^{-T} \mathbf{P}^T \mathbf{P} \mathbf{A}^{-1})), \quad (8)$$

where  $\Lambda_{\max}$  represents the largest eigenvalue of  $\mathbf{A}^{-T} \mathbf{P}^T \mathbf{P} \mathbf{A}^{-1}$ ,  $\eta$  is the part of the penalty parameter  $\tau$  in Eq. (5) (Leeuwen and Herrmann, [2015](#)).

### 2.3. Solving procedure with modified Sobolev space regularization-based quadratic penalty method

The gradient of the objective function in FWI typically comprises two main components when doing the optimization: a data error item and a regularization item. The data error item minimizes the discrepancy between simulated and observed waveforms, while the regularization term serves to control the smoothness and stability of the solution, prevent overfitting, and address noise and uncertainties in the data. The influence of Tikhonov regularization (Asnaashari et al., [2013](#)) and TV regularization in inversion problems is well-known (Brandsberg-Dahl et al., [2017](#)); Tikhonov regularization tends to favour smoother models which enhance continuity, whereas TV regularization is known to suffer from the staircase effect (Wang and Feng, [2021](#)). However, more advanced variable regularization methods with adjustable norm paths are rarely considered for adoption in FWI, due to the complexity of the theory. But for practical production in tunnel advance prediction, adjustable regularization that can be adapted to different geological conditions is obviously a better choice. In this paper, based on the reconstruction of wavefields, we consider using a  $W_p^1$  norm in Sobolev spaces to balance data fitting accuracy with the physical interpretability of the model, simultaneously enhancing the stability and robustness of the inversion process (Adams and Fournier, [2003](#); Fischer and Steinwart, [2020](#)). With the addition of the regularisation term, Eq. (5) can be expanded:

$$F(\mathbf{m}) = \Phi(\mathbf{m}) + \Psi(\mathbf{m}), \quad (9)$$

where  $\Phi(\mathbf{m})$  is the quadratic penalty objective term with a data error item and a wave equation item based on the quadratic penalty method,  $\Psi(\mathbf{m})$  is the regularization term. In the left side term of Eq. (9), the closed-form solution of the eliminated wavefield  $\mathbf{u}^{n+1}$  of the quadratic penalty has been shown in Eq. (6). Then, the estimated wavefield is brought back into the optimization, and a new inter-loop of misfit computation procedure can be obtained the model parameter variables according to the alternating principle:

$$\begin{aligned} \Phi(\mathbf{m}^n) = & \sum_{i=1}^{N_a} \sum_{j=1}^{N_b} (\mathbf{P}\mathbf{u}_{i,j}^{n+1} - \mathbf{D}_{i,j})^H (\mathbf{P}\mathbf{u}_{i,j}^{n+1} - \mathbf{D}_{i,j}) + \\ & \tau \sum_{i=1}^{N_a} \sum_{j=1}^{N_b} (\mathbf{A}_{i,j}(\mathbf{m}^n)\mathbf{u}_{i,j}^{n+1} - \mathbf{S}_{i,j})^H \times (\mathbf{A}_{i,j}(\mathbf{m}^n)\mathbf{u}_{i,j}^{n+1} - \mathbf{S}_{i,j}), \end{aligned} \quad (10)$$

where  $N_a$  is the number of angle frequencies,  $N_b$  is the number of sources in an acquisition system.  $(\cdot)^H$  denotes the Hermitian transpose operation (Feng et al., 2022). Eq. (6) and Eq. (10) ensure that the wavefield computation is not solely based on solving PDE, i.e., it does not rely exclusively on the mathematical methods of solving full PDE (Grote et al., 2014). Instead, it incorporates more extensive analysis and utilization of actual observational data and involves implementing data-driven models to enhance the accuracy of the wavefield estimation. The advantage is that accuracy is guaranteed and convergence is faster in the case of approximate solutions computed in a computationally acceptable solution space.

Eq. (9) on the right side includes a regularization term that is used to control the smoothness and stability of the solution, prevent overfitting, and address noise and uncertainties in the data. Consequently, the original optimization problem can be reconstructed as follows:

$$J(m) = \Phi(\mathbf{m}) + \beta \|\mathbf{m}\|_{w_p^1}, \quad (11)$$

where  $\beta$  is a regularization parametric operator,  $\|\cdot\|_{w_p^1}$  is  $w_p^1$  norm in Sobolev space. In the  $w_p^1$  norm,  $p$  is a selectable value that is not less than zero, depending on the physical significance and

the required strength of regularization. When  $p = 1$ , the  $w_p^1$  norm exhibits characteristics of the TV norm, while  $p = 2$ , it exhibits characteristics of the Tikhonov regularization. If  $p$  value lies between these values, particularly when  $p = 0.5$ , it displays features similar to those of the minimum gradient support (MGS) stabilizer (Kazei et al., [2017](#)). We give a multi-view schematic of the visualisation and simulation of the  $w_p^1$  norm in **Fig. 1**.

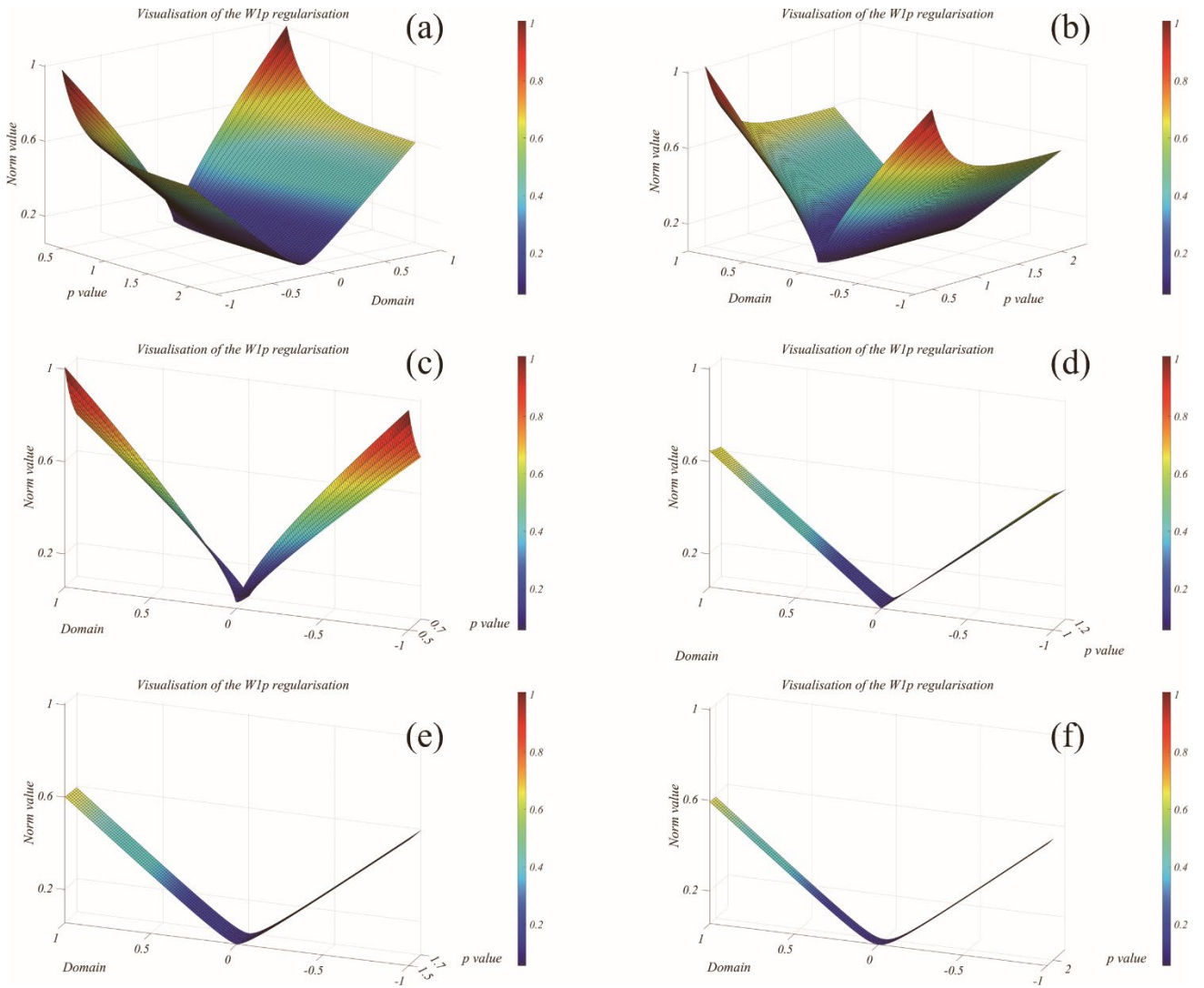


**Fig. 1.** Visualization and simulation of the  $W_p^1$  regularization. (a)  $p$  values ranging from 0.5 to 2, the azimuth angle (az) is 50, and the elevation angle (el) is 15, (az: 50, el: 15). (b)  $p$  values ranging from 0.5 to 2, the az is negative 50, the elevation angle (el) is 15, (az: -50, el: 15). (c)  $p$  values ranging from 0.5 to 0.7, which exhibits the

characteristics of the 0.5 norm. (d)  $p$  values ranging from 1 to 1.2, which exhibits the characteristics of TV regularization. (e)  $p$  values ranging from 1.5 to 1.7, which exhibits the characteristics of the 1.5 norm. (f)  $p$  value is equal to 2, which exhibits the characteristics of the Tikhonov regularization.

As an adjustable and flexible norm, the  $w_p^1$  norm exhibits various characteristics when  $p$  taking different values. This figure illustrates how the  $w_p^1$  norm of a two-dimensional vector changes across different  $p$  values (ranging from 0.5 to 2) and the domain (varying from -1 to 1). Each  $p$  value corresponds to a specific method of norm calculation, and this three-dimensional view demonstrates the dynamic variations of the norm under different parameters. Specifically, **Fig. 1(a)** shows a side view at an azimuth angle of 50 and an elevation angle of 15, whereas **Fig. 1(b)** presents a side view at an azimuth angle of negative 50 and an elevation angle of 15. **Fig. 1(c)-(f)** display side views for  $p$  values of 0.5, 1, 1.5, and 2, respectively. It can be observed that as  $p$  approaches 2, the  $w_p^1$  norm tends towards a convex regularization known as Tikhonov regularization; when  $p$  is close to 0.5, the  $w_p^1$  norm exhibits a distinct concave. At  $p$  equal to 1, the  $w_p^1$  norm aligns with TV regularization, remaining convex because a convex function's value on any line segment between two points is less than or equal to the average of the function values at the endpoints. Thus, the  $p$  parameter of the  $w_p^1$  function maintains its convex property as long as it is greater than or equal to 1, ensuring that the optimization process in FWI stays largely convex, which helps avoid the impact of local minima.

The revised and optimized formula of the  $w_p^1$  norm is as follows:

$$\|\mathbf{m}\|_{w_p^1} = \left( \int_{\Gamma} |\mathbf{m}(x)|^p dx + \int_{\Gamma} (\nabla \mathbf{m}(x) \cdot \nabla \mathbf{m}(x) + \sigma)^{p/2} dx \right)^{1/p}, \quad (12)$$

where  $\Gamma$  denotes the model space definition domain,  $\mathbf{m}(x)$  denotes the model parameter at position  $x$  and  $\nabla \mathbf{m}(x)$  denotes the gradient of the model parameter. Eq. (12),  $\sigma$  is a tiny and positive value for ensuring the numerical stability of the mathematical expressions. Physically, the

purpose of adding  $\sigma$ , which helps ensure that calculations remain stable even in regions where changes in the model parameter values are minimal, thus preventing potential numerical errors or instabilities, is to avoid computational issues when the gradient  $\nabla \mathbf{m}(x)$  is close to zero. Consequently, the gradient of the Eq. (11) can be implicitly expressed as:

$$\nabla_{\mathbf{m}} J(\mathbf{m}) = \nabla_{\mathbf{m}} \Phi(\mathbf{m}) + \beta \nabla_{\mathbf{m}} \|\mathbf{m}\|_{w_p^1}, \quad (13)$$

Eq. (13) integrates the soft constraint containing data error item and wave equation item, and regularization terms, controlling the discrepancy between simulated and observed data as well as the smoothness and complexity of the model. The model parameters are updated via a multi-scale strategy, aiming to prevent overfitting and enhance the physical interpretability of the model. According the Eq. (3), Eq. (5) and Eq. (6), the gradient of the misfit penalty term can be expressed as:

$$\nabla_{\mathbf{m}} \Phi(\mathbf{m}) = \sum_{i=1}^{N_a} \sum_{j=1}^{N_b} \omega_{i,j}^2 \text{diag}(\mathbf{u}_{i,j}^{n+1})^T \left( \mathbf{A}_{i,j}(\mathbf{m}^n) \mathbf{u}_{i,j}^{n+1} - \mathbf{S}_{i,j} \right), \quad (14)$$

the above equation computes the gradient of the quadratic penalty across multiple source and receiver configurations, capturing the model's response to various seismic sources and receivers and their discrepancies with observational data. This process aims to precisely quantify changes in model parameters, thus guiding the direction of parameter updates. Further, the regularization term's local gradient of the function about the  $W_p^1$  norm can also be evaluated as follows:

$$\nabla_{\mathbf{m}} \|\mathbf{m}\|_{w_p^1} = \|\mathbf{m}\|_{w_p^1}^{1-p} \left( p |\mathbf{m}(x)|^{p-2} \mathbf{m}(x) + p (\nabla \mathbf{m}(x) \cdot \nabla \mathbf{m}(x) + \sigma)^{(p/2)-1} \nabla \mathbf{m}(x) \right), \quad (15)$$

within this framework, the gradient of the  $W_p^1$  norm, and the regularization operator  $p$  can be adjusted, which facilitates flexible control over the model's smoothness and numerical stability. Consequently, the proposed method proves particularly effective for identifying geological models that require high continuity and stability, such as faults, especially in scenarios involving the prediction of faults that may be encountered in advance during tunnel excavation processes. In the

proposed improved FWI framework, the updating process of the model parameters can be carried out using the alternating minimisation algorithm:

$$\mathbf{m}^{n+1} = \arg \min_{\mathbf{m}_{\min} \leq \mathbf{m} \leq \mathbf{m}_{\max}} \beta \|\mathbf{m}\|_{w,p} + \tau \|\omega^2 \text{diag}(\mathbf{u}^{n+1}) - \mathbf{S} + \Delta \mathbf{u}^{n+1}\|_2^2, \quad (16)$$

this update process allows for the computation and accumulation of wavefields independently and alternating without storing all wavefields. The system is strictly diagonal, simplifying the computational process.

In summary, the proposed algorithm integrates various benefits of conventional methods and the Lagrangian approach to construct and solve optimization problems, thereby extending the gradient search space. Additionally, the algorithm incorporates a flexible, adjustable regularization method to maintain a balance between sharp and smooth updates in FWI, mitigating nonlinearity and the potential for local minima while enhancing denoising capabilities. We will further elucidate the effectiveness and superiority of the proposed methods through comparison examples in subsequent sections.

### 3. Tunnel synthetic numerical simulation and inversion of a single fault structure

As a well-established geophysical exploration technique, FWI has been extensively applied in petroleum and natural gas exploration, especially in offshore salt environments, achieving high-resolution exploration objectives (Morgan et al., [2013](#)). However, its application in tunnel advance prediction and near-surface engineering is still limited (Liu et al., [2023](#)). This limitation is primarily due to the resolution of FWI being constrained by the wavelength of the seismic waves used; in tunnel detection, the feature sizes that need to be identified (such as tunnel diameters or thin faults) may be smaller than the wavelength of the seismic waves, thereby reducing the effectiveness of FWI in these applications (Klotzsche et al., [2019](#)). Additionally, the acquisition of seismic data in tunnel engineering may be restricted because the environment is often spatially confined and challenging for the deployment of sufficient seismic sensors, leading to diminished data quality

(Riedel et al., [2023](#)). Another crucial factor is noise interference in tunnel environments. In FWI applications, noise issues are particularly critical as FWI relies on high-quality seismic data to accurately invert underground structures. Compared to offshore applications, noise sources and impacts differ significantly in tunnel prediction or near-surface applications. In urban or industrial areas, seismic exploration is typically affected by vibrations from vehicles, machinery, and other construction activities (Athanasopoulos and Pelekis, [2000](#)). Moreover, near-surface geological layers often exhibit significant variability, including discontinuities, voids, and fractures, which can scatter and absorb seismic waves, increasing background noise (Francesse et al., [2002](#)).

Considering these limitations, we have specifically designed a numerical model with small-scale tilted fault structures and incorporated significant signal-to-noise ratio (SNR) noise interference to simulate the complex environment of tunnel advance prediction. This section is intended to test the effectiveness of the algorithm proposed in this paper for inversion in complex and constrained environments of tunnel advance prediction.

### 3.1. Acquisition system and forward modelling

This paper initially considers a two-dimensional fault model for tunnel advance prediction.

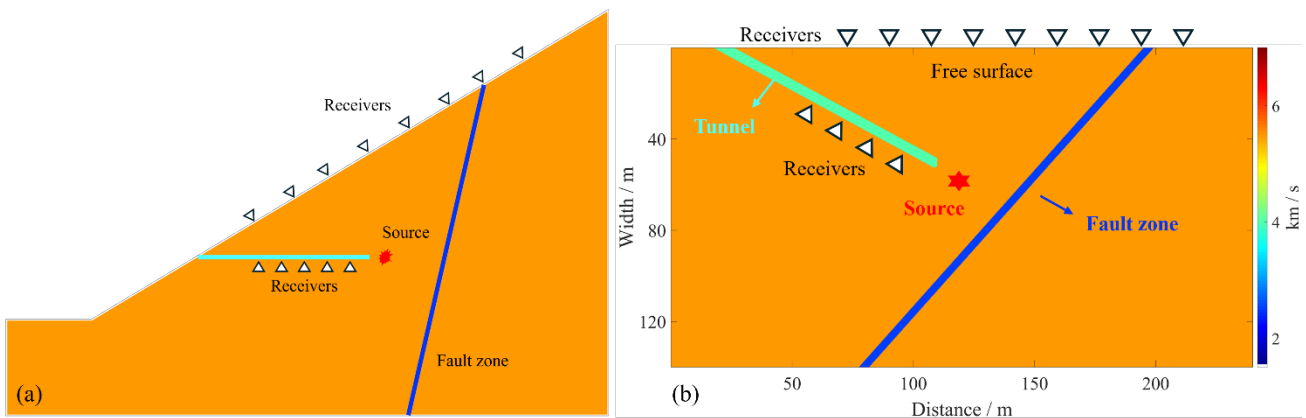


**Fig. 2.** Schematic of the model structure. (a) Tunnel structural model with an inclined fault. (b) The modelling

results after tilting the schematic **Fig. 2(a)**, the top of the modelling is a free surface to simulate the real ground surface (the number of receivers in the schematic does not represent the real number of receivers).

In **Fig. 2(a)**, the model is rotated such that the angle between the tunnel and the free surface is 30 degrees to facilitate better modelling. The tunnel diameter is set at 5 m, and the starting position of the tunnel in the model is 20 m from the left side origin. Additionally, a fault structure is located on the right side of the model, with a thickness of 5 m and a fault velocity of 2.5 m / s. The fault starts at a horizontal distance of 80 m. **Fig. 2(b)** illustrates the schematic of the modelling. The overall size of the model is 240 m  $\times$  140 m, with a total area of 33600 m<sup>2</sup>. The surrounding rock velocity is 5.5 m / s. In our system configuration, we deploy only two seismic sources positioned in front of the tunnel face, without any time delay. The minimal number of sources is designed to minimize the destructive impact caused by the sources and to increase the inversion challenge, simulating extreme conditions for result comparison. Additionally, considering the spatial constraints typically associated with tunnel environments, which may limit the deployment of sufficient seismic sensors, we opt not to place receivers at the tunnel roof. Instead, we place only 7 receivers at the tunnel bottom. Due to the absence of spatial and environmental restrictions at the free surface of the overlying rock mass, we can deploy a large number of receivers; specifically, we place 26 equally spaced receivers, each separated by 6.67 m.

In this study, we implement absorbing boundary conditions on the left, right, and bottom sides of a two-dimensional isotropic model, while the top surface is treated as a free surface to simulate the actual properties of the geological surface (Takekawa and Mikada, [2016](#)). We utilize acoustic FWI to accurately invert fault structures.



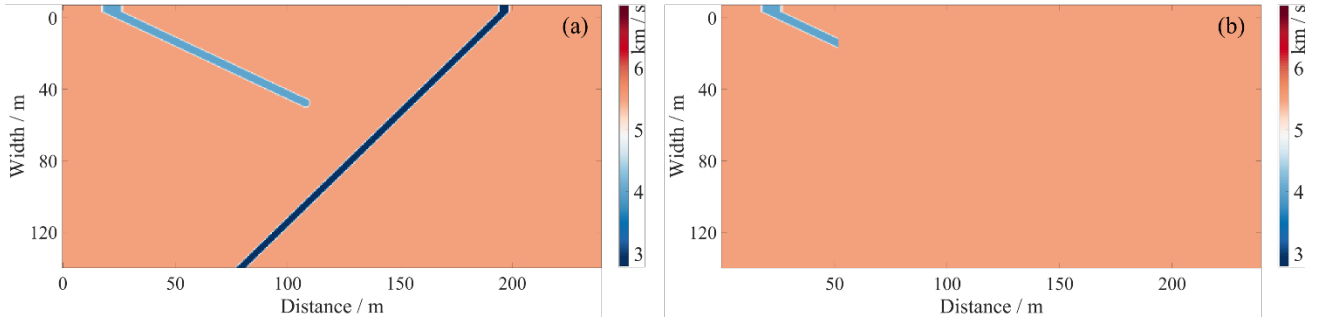


**Fig. 3.** Modelling of a fault structure for tunnel advance prediction. (a) Benchmark of the model with a tilted fault. (b) The initial model of the benchmark. The tunnel structure was removed for inversion self-consistency testing.

As depicted in **Fig. 3(a)** represents the true modelled structure, and **Fig. 3(b)** shows the initial velocity model. Notably, the initial model does not include the known tunnel structure; this omission is intentional to allow for the simultaneous simulation of the tunnel during subsequent modelling. This approach enables us to compare the inverted tunnel results with the true model, serving the purpose of validating inversion self-consistency. In the forward modelling phase, we discretize the model using the finite difference method with a grid size of 6.67m, comprising a total of 77400 cells. We use a frequency-domain forward modelling algorithm and a multi-scale inversion strategy to mitigate local minima and alleviate nonlinearity. Our frequency stepping approach increases each subsequent inversion frequency by a factor of 1.2, enhancing the efficiency and stability of the inversion process.

Subsequently, we perform a forward process of the benchmark to obtain the real part of the forward wavefield as shown in **Fig. 4(a)**, **Fig. 4(b)** is the imaginary part of the forward wavefield. A forward process of the initial model to obtain the real part of the background wavefield as shown in **Fig. 4(c)**, **Fig. 4(d)** is the imaginary part of the initial background wavefield.

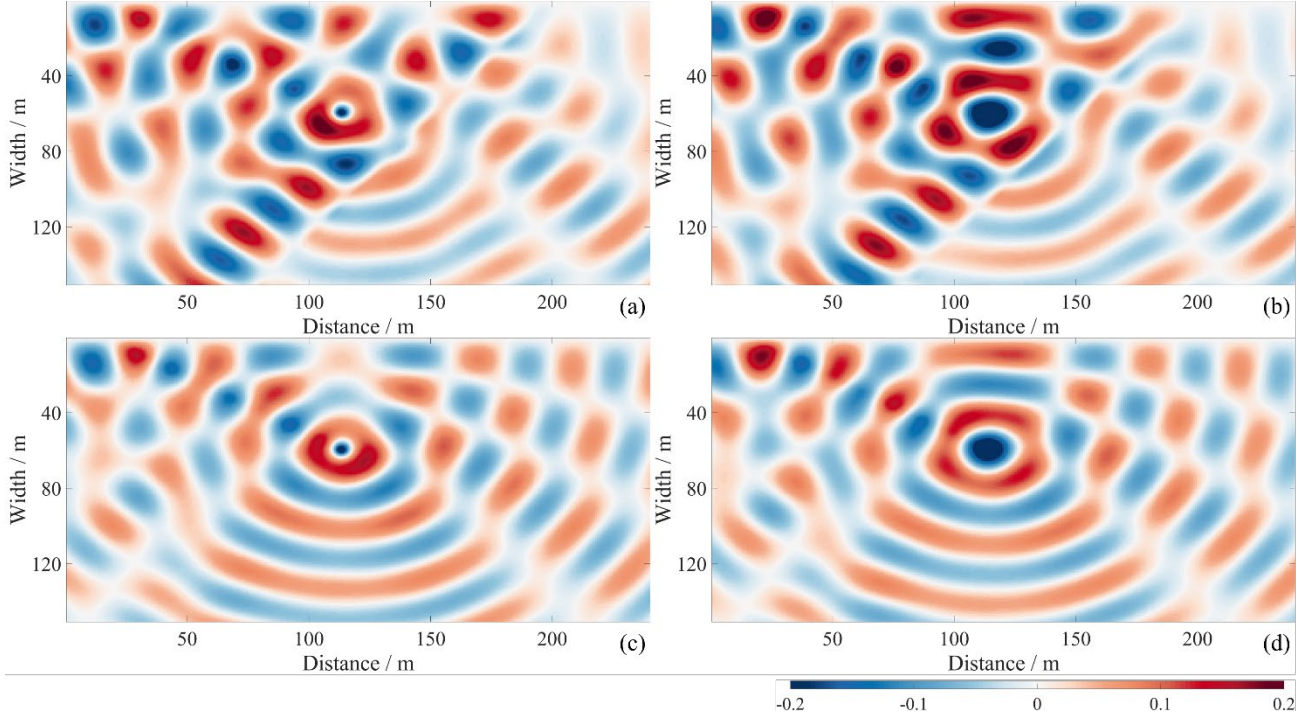


**Fig. 4.** Forward wavefield information. (a) The real part of the forward wavefields. (b) The imaginary part of the forward wavefields. (c) The real part of the initial background wavefield. (d) The imaginary part of the background wavefield.

Another key factor to consider is noise interference in tunnel environments. Particularly in applications of tunnel advance prediction or near-surface surveying, especially in urban or industrial areas, seismic exploration is often affected by vibrations from vehicles, machinery, and other construction activities (Li et al., 2024b). Thus, it is crucial to consider the significant impact of noise on the inversion process:

$$\text{SNR} = 20 * \text{Log}_{10} \left( \frac{\|\mathbf{D}\|_2}{\|\mathbf{E}\|_2} \right), \quad (17)$$

where the  $\mathbf{E}$  is the noise. We consider the impact of adding 4.9 dB of random noise to the benchmark wavefield, as shown in Fig. 5. Fig. 5(a) displays the real part of the clean source-receiver wavefield, where the vertical axis represents the two sources and the horizontal axis corresponds to 33 receivers.

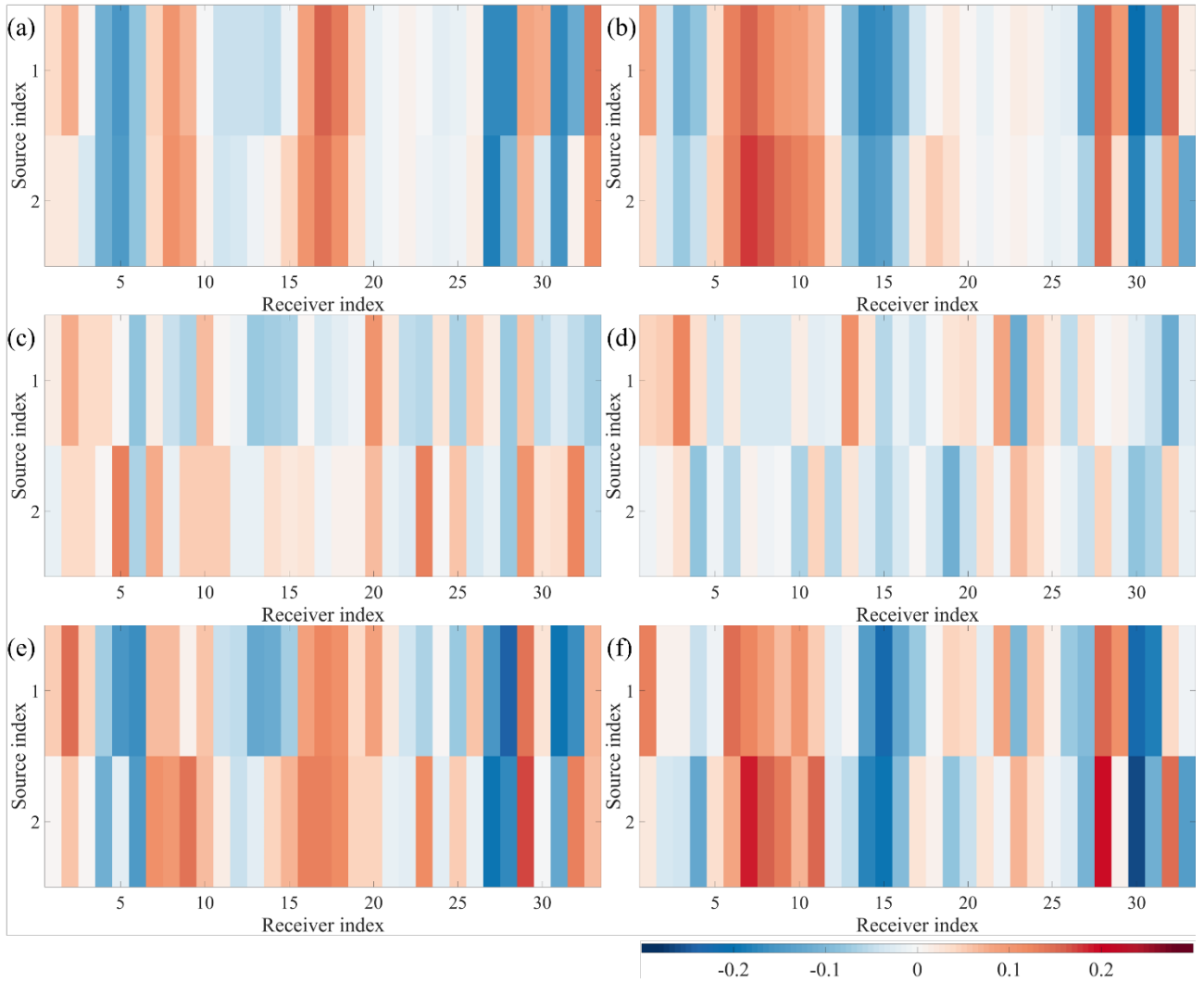


**Fig. 5.** Source receiver wavefield for the tunnel model. (a) The real part of the clean wavefield without noise component. The vertical coordinate explicit acquisition system consists of two seismic sources, horizontal coordinates from 1 to 26 for receivers on the free surface and from 27 to 33 for receivers on the tunnel floor. (b) The imaginary part of the clean wavefield without noise component. (c) The real part of the random noise. (d) The imaginary part of the random noise. (e) The real part of the wavefield with random noise as a means for further inversion. (f) The imaginary part of the wavefield with random noise as a means for further inversion.

Receivers 1-26 are located on the free surface, while receivers 27-33 are positioned on the tunnel floor. **Fig. 5(b)** displays the imaginary part of the clean source-receiver wavefield. **Fig. 5(c)**

illustrates the 4.9 dB random noise. **Fig. 5(d)** illustrates the imaginary part of the noise. **Fig. 5(e)** shows the real part of the source-receiver wavefield information after the noise was added. **Fig. 5(f)** shows the imaginary part of the source-receiver wavefield information after the noise was added.

### 3.2. Optimization

Before conducting the final inversion tests, a critical and non-negligible issue is the selection of the penalty parameter  $\tau$  in Eq. (5). As previously mentioned, in the proposed method, the penalty parameter  $\tau$  should be represented by the maximum eigenvalue of the matrix  $\mathbf{A}^{-T}\mathbf{P}^T\mathbf{P}\mathbf{A}^{-1}$  in Eq. (8). However, depending on practical application circumstances, it is necessary to scale the maximum eigenvalue to a certain extent to ensure reaching a suitable magnitude's stationary point of the Lagrangian function within a predefined scaling range (Abdouliev et al., 2005). The size of the scaling parameter  $\gamma$  directly affects the convergence and stability of the algorithm. Mathematically, as  $\gamma$  approaches infinity, the solution of the penalty method tends to satisfy all constraints, but this may also lead to the deterioration of the condition number of the Hessian matrix, making computations unstable (Banerjee et al., 2013). To ensure that the algorithm reaches the expected convergence accuracy within a finite number of iterations, the  $\gamma$  value should be as small as possible to enforce the constraints while avoiding algorithmic instability. In this section, we will compare and test several different  $\gamma$  values to discuss in detail the impact of the penalty parameter on the quadratic penalty method.

Firstly, the performance of four different scaling factors,  $\gamma$ , is tested under the specific model conditions presented in this paper. **Fig. 6** displays the inversion results after 20 iterations at 3.6 Hz for each scaling factor. **Fig. 6(a)** corresponds to  $\gamma = 1e-2$ , **Fig. 6(b)** to  $\gamma = 1e-1$ , **Fig. 6(c)** to  $\gamma = 1e0$ , and **Fig. 6(d)** to  $\gamma = 1e2$ .

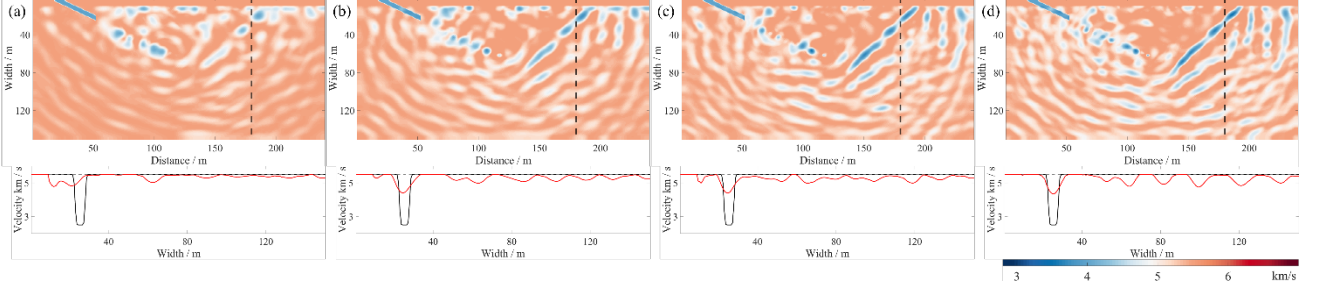


**Fig. 6.** Comparison of inversion tests with different scaling factors  $\gamma$  for maximum eigenvalues  $\mathbf{A}^{-T}\mathbf{P}^T\mathbf{P}\mathbf{A}^{-1}$ . (a)  $\gamma = 1e-2$ . (b)  $\gamma = 1e-1$ . (c)  $\gamma = 1e0$ . (d)  $\gamma = 1e2$ . In the inversion results, the black dashed line represents the specific locations of a set of velocity contrasts we sampled. Directly below the inversion results, a set of vertical velocity contrasts is displayed, where the black solid line corresponds to the benchmark velocity, the red solid line to the inverted velocity, and the grey dashed line to the initial velocity. As the scaling factor increases, leading to a smaller reciprocal of the scaling factor, the inversion results tend to become unstable due to the dominance of the data mismatch term. Conversely, with smaller scaling factors, resulting in a larger reciprocal of the scaling factor, the inversion results are more stable as the wave equation term becomes more predominant.

Theoretically, as the scaling factor increases, the inversion results tend to become unstable due to a smaller reciprocal of the scaling factor, with the data mismatch term becoming dominant. This effect is observed as an increase in artefacts with larger  $\gamma$  values. Conversely, smaller scaling factors result in more stable inversion outcomes, where the larger reciprocal enhances the dominance of the wave equation term, also reflected in the increasing clarity of artefacts with larger  $\gamma$  values. These observations confirm that excessively large scaling factors, or very small reciprocals of  $\gamma$ , can diminish the influence of the wave equation term, causing the optimization to degrade toward conventional LS. However, excessively small  $\gamma$  values may also lead to underfitting. Thus, subsequent tests will compare both  $\gamma = 1e-2$  and  $\gamma = 1e-1$  scenarios with conventional algorithms to evaluate their performance. Additionally, the convergence process of the largest eigenvalue of the matrix  $\mathbf{A}^{-T}\mathbf{P}^T\mathbf{P}\mathbf{A}^{-1}$  under four scaling factor scenarios was compared, as shown in **Fig. 7**.

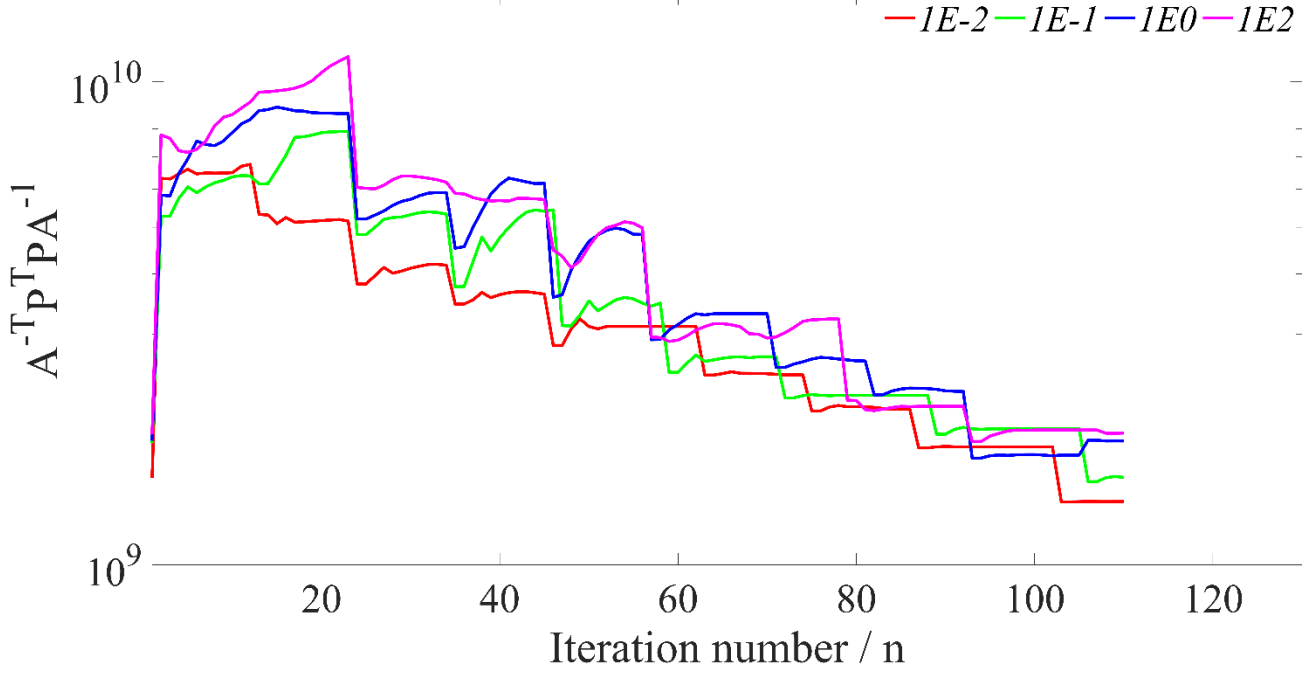


**Fig. 7.** Maximum eigenvalue curve of  $\mathbf{A}^{-T}\mathbf{P}^T\mathbf{P}\mathbf{A}^{-1}$  in relation to the penalty parameter  $\tau$  in Eq. (8). The curves are shown for three different scaling levels,  $\gamma = 1e-2$  in red,  $\gamma = 1e-1$  in green,  $\gamma = 1e0$  in blue and  $\gamma = 1e2$  in magenta.

The adoption of a multi-scale inversion strategy means that the size of the penalty term parameter can significantly influence the smoothness of the convergence process. This influence is manifested by phenomena similar to spikes, which are not caused by typical noise-induced instability in the data but result from frequency switching leading to re-convergence (Chowdhery et al., [2023](#)). Therefore, even if it is not possible to drop back down at a single frequency, the impact on the convergence process remains limited. As observed, smaller scaling factors lead to faster convergence of the  $\mathbf{A}^{-T}\mathbf{P}^T\mathbf{P}\mathbf{A}^{-1}$  matrix. Furthermore, as derived in Appendix A, faster convergence indicates a higher model update rate.

Additionally, the relative impacts of the data mismatch term and the wave equation term were compared across four scaling factors after 20 iterations, as illustrated in **Fig. 8**.

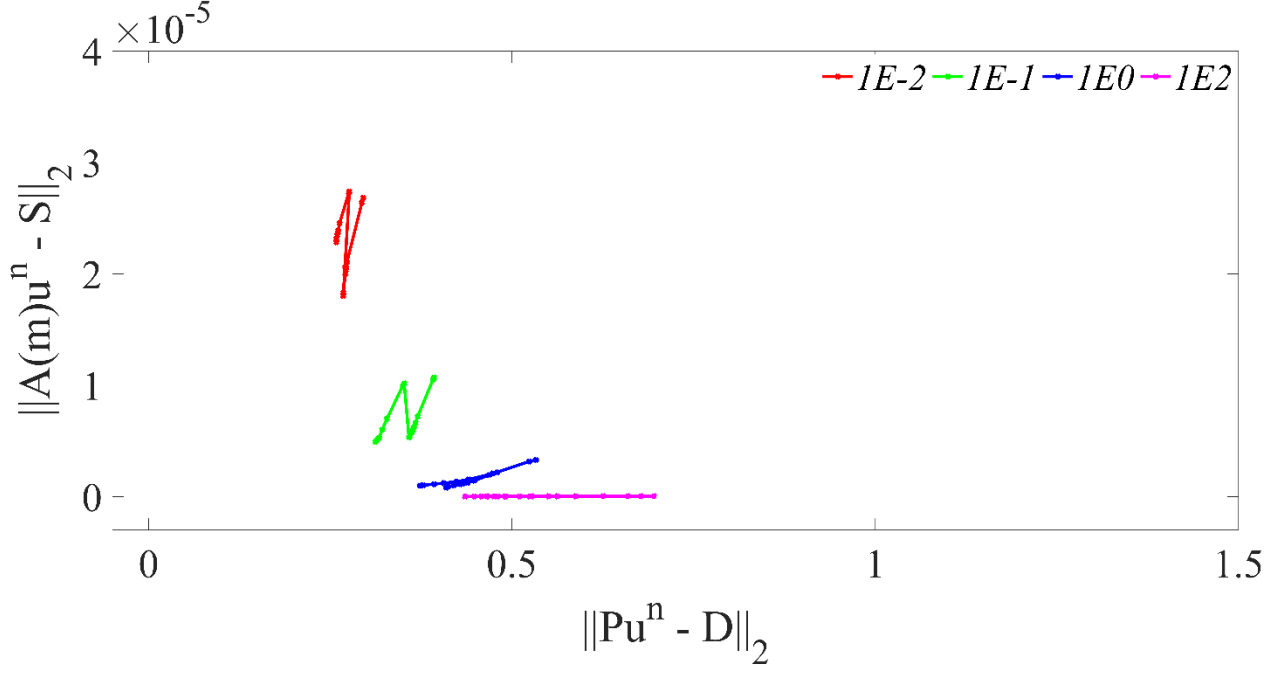


**Fig. 8.** Relative importance of the data mismatch term and the wave equation penalty term in the initial stage of the inversion. The curves are shown for four different scaling levels,  $\gamma = 1e-2$  in red,  $\gamma = 1e-1$  in green,  $\gamma = 1e0$  in blue and  $\gamma = 1e2$  in magenta. Smaller scaling factors can ensure that both terms maintain convergent behaviour simultaneously. At  $\gamma = 1e-2$ , the data mismatch term declines rapidly, but the wave equation term does not reduce to the same level as the data mismatch term, suggesting the possibility of the wave equation term falling into a local minimum. At  $\gamma = 1e-1$ , the wave equation term converges slightly faster than the data term, and both decline synchronously. At  $\gamma = 1e0$ , the two terms maintain nearly identical speeds. However, at  $\gamma = 1e2$ , the wavefield term's correlation with the data mismatch term is too small, potentially leading to a scenario where the data term converges independently. Importantly, at this scaling, the data mismatch term does not reduce to a level nearly similar to that of the wave equation term and declines noticeably slower, indicating that the data mismatch term has fallen into a local minimum.

The most significant finding is that smaller scaling factors ensure that both terms maintain synchronous convergence behaviour. At  $\gamma = 1e-2$ , the data mismatch term declines rapidly, but the wave equation term does not reduce to the same level as the data mismatch term, suggesting the possibility of the wave equation term falling into a local minimum. At  $\gamma = 1e-1$ , the wave equation term converges slightly faster than the data term, and both decline synchronously. At  $\gamma = 1e0$ , the

two terms maintain nearly identical speeds. However, at  $\gamma = 1e2$ , the wavefield term's correlation with the data mismatch term is too small, potentially leading to a scenario where the data term converges independently. Importantly, at this scaling, the data mismatch term does not reduce to a level nearly similar to that of the wave equation term and declines noticeably slower, indicating that the data mismatch term has fallen into a local minimum. Finally, the convergence processes of the two terms over iterations for four different scaling factors are presented in **Fig. 9**.

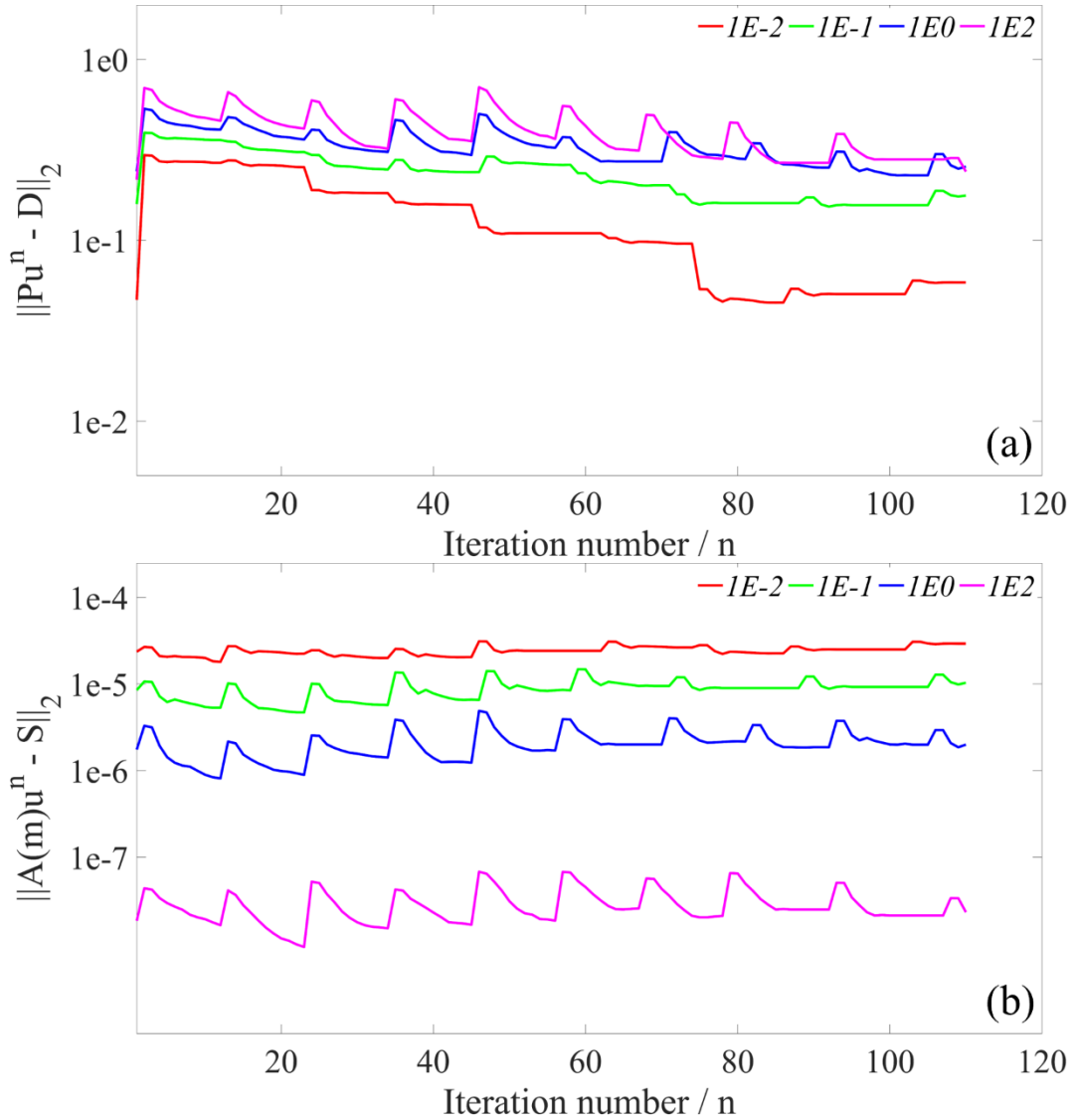


**Fig. 9.** Sensitivity analysis of different parameters  $\tau$ . (a) Convergence process of the data mismatch penalty term of the objective function. (b) Convergence process of the wave equation penalty term of the objective function. Construction of the objective function according to Eq. (5). The curves are shown for four different scaling levels,



$\gamma = 1e-2$  in red,  $\gamma = 1e-1$  in green,  $\gamma = 1e0$  in blue and  $\gamma = 1e2$  in magenta. Additionally, the larger the regularization parameter, the more pronounced the loss spike phenomenon becomes. For the specific model discussed, iterations fewer than 100 are sufficient. Excessive iterations have resulted in a very slight degree of overfitting.

The results consistently demonstrate that for the specific model discussed in this paper, iterations of fewer than 100 are sufficient. Excessive iterations have resulted in a very slight degree of overfitting.

### *3.3. Inversion and interpretation*

During the inversion phase, we use the limited-memory Broyden–Fletcher–Goldfarb–Shanno (L-BFGS) algorithm (Liu and Nocedal, [1989](#)). Compared to the steepest descent (SD) and conjugate gradient methods (CG), L-BFGS converges faster. While the SD method is simple and updates in the direction of the current gradient, which is often suboptimal and prone to local minima, the CG method, which is based on the conjugacy of two gradients, depends on the condition number and other factors. In contrast, L-BFGS utilizes curvature information (approximating the Hessian matrix), offering a balanced optimization approach in terms of memory usage, convergence speed, and adaptability, particularly suited for large-scale optimization challenges. In brief, L-BFGS more effectively identifies the correct descent direction, thus accelerating convergence.

Subsequently, we present the FWI results obtained using three different algorithms as shown in **Fig. 10**,

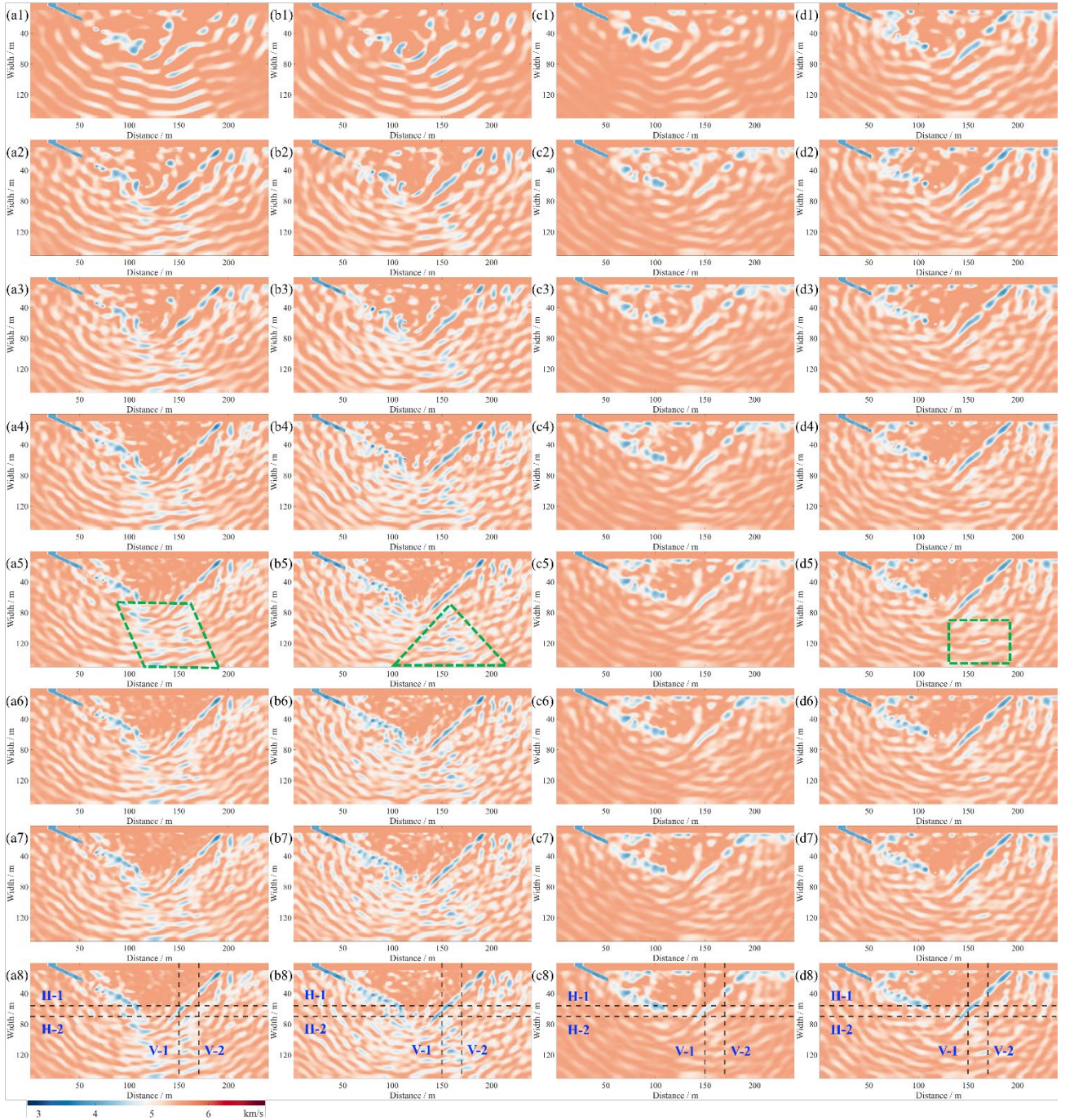


**Fig. 10.** Inversion results comparison. (a1)-(a7) Tikhonov - FWI regularization at 3.0 Hz, 3.6 Hz, 4.0 Hz, 4.8 Hz, 5.8 Hz, 6.4 Hz and 7.1 Hz. (b1)-(b7) TV - FWI in the same frequency range. (c1)-(c7) Proposed method in the same frequency range and  $\gamma = 1e-2$ . (d1)-(d7) Proposed method in the same frequency range but  $\gamma = 1e-1$  case. The green polygons identify the areas of low-velocity artefacts. Horizontal (a8)-(d8) are direct copies from (a7)-(d7). The black dashed lines indicate the target locations for subsequent velocity profile analyses. V-1 and V-2 represent two sets of vertical sample traces located at 150 m and 170 m, respectively, while H-1 and H-2 represent

two sets of horizontal sample traces located at 52 m and 65 m, respectively.

where **Fig. 10(a1)-(a7)** are the inversion results from Tikhonov regularization-based FWI at frequencies of 3.0 Hz, 3.6 Hz, 4.0 Hz, 4.8 Hz, 5.8 Hz, 6.4 Hz, and 7.1 Hz. **Fig. 10(b1)-(b7)** depict the results from TV regularization-based FWI at the same frequencies, **Fig. 10(c1)-(c7)** display the outcomes from the proposed method-based FWI at  $\gamma = 1e-2$ , also at the same frequencies, and **Fig. 10(d1)-(d7)** display the outcomes from the proposed method-based FWI at  $\gamma = 1e-1$ , also at the same frequencies. All results utilize the same colour map. From the inversion results of the three different algorithms, it is evident that the Tikhonov regularization-based FWI can identify fault and tunnel structures, but performs poorly in the inversion of deep, uniform media, exhibiting significant and numerous artefacts, which are theoretically influenced by noise, cycle-skipping, and local minima, especially over large areas of homogeneous media. Given that the inversion frequency in FWI should not be set too high, and considering the critical importance of low-frequency data for large areas of homogeneous media, the impact of high-wavenumber artefacts must be considered when effective low-frequency data is often unavailable. Furthermore, the choice of regularization and its parameters is crucial; if the regularization parameter is set too low, it complicates the inversion of fault structures and overly smooths the inversion features. Therefore, this also demonstrates that for nonlinear optimization problems, an appropriate choice of regularization is extremely important. Additionally, the inversion results based on TV regularization, as shown in the middle column of **Fig. 10**, clearly exhibit more pronounced and discontinuous artefacts, theoretically due to the L1 norm basis of TV regularization. Although the sparse constraint of the L1 norm excels in noise reduction while preserving image edges and structural information, crucial for maintaining clear geological interfaces in geophysical inversion, its non-differentiability at the origin can lead to numerical instability in the optimization process, particularly in contexts involving inherently smooth or homogeneous media. Sparse constraints tend to promote gradient sparsity, potentially introducing unnecessary gradient variations within uniform regions, thereby generating artefacts that manifest as unrealistic boundaries or structures. In contrast, the results from the improved algorithm proposed in

this paper, as shown in the right two columns of **Fig. 10**, appear more stable, with clearer inversion of faults and tunnel structures. Importantly, they exhibit superior performance in the inversion of uniform media without apparent artefact structures, thus avoiding misinterpretation. Theoretically, this advantage is due to the superiority of the quadratic penalty method and Sobolev space norms. Specifically, the calculations of the wavefield and adjoint operators in the algorithm proposed in this paper have been modified. Furthermore, the  $W_p^1$  regularization utilized in this example, being a non-L1 norm class, ensures differentiability at the origin, and while enhancing regularization effects, avoids excessive artefact generation. The green boxes identify obvious artefact locations in the inversion results of the three methods for the homogeneous medium part at the depth of the model. Horizontal **Fig. 10(a8)-(d8)** are direct copies from **Fig. 10(a7)-(d7)**. The black dashed lines indicate the target locations for subsequent velocity profile analyses. V-1 and V-2 represent two sets of vertical sample traces located at 150 m and 170 m, respectively, while H-1 and H-2 represent two sets of horizontal sample traces located at 52 m and 65 m, respectively.

Additionally, we provide some analysis of the inversion results. **Fig. 11** shows the final gradients of three different algorithms. **Fig. 11(a)** represents the final gradient of the Tikhonov regularization inversion process, **Fig. 11(b)** is from the TV regularization, and **Fig. 11(c)** is from the improved algorithm proposed at  $\gamma = 1e-2$  in this paper. **Fig. 11(d)** is from the improved algorithm proposed at  $\gamma = 1e-1$ .



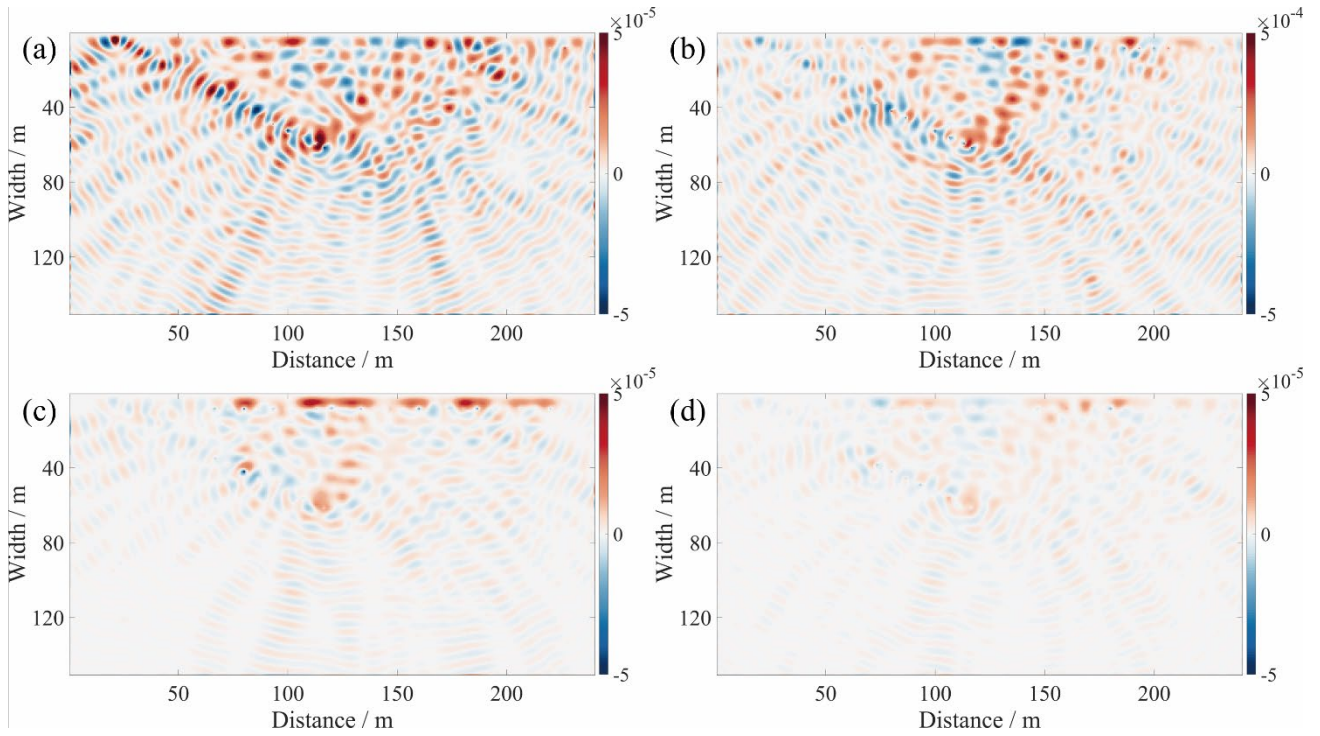


**Fig. 11.** The final residual gradient of the inversion. (a) FWI based on the Tikhonov regularization. (b) FWI based on TV regularization. (c) FWI based on the proposed method and  $\gamma = 1e-2$ . (d) FWI based on the proposed method but  $\gamma = 1e-1$  case. The gradients of **Fig. 11(b)** and others vary by one order of magnitude, with the minimum and maximum gradient ranging from **Fig. 11(b)** at  $[-5e-4, 5e-4]$  and that of others at  $[-5e-5, 5e-5]$ .

Notably, the colour map's maximum value for TV regularization is an order of magnitude higher than the other two algorithms. From the final gradients, it is evident that the conventional algorithms still exhibit significant residual gradients at the bottom of the model, which is a homogeneous medium, due to the effects of strong noise and artefacts. Conversely, the improved algorithm shows no noticeable residual gradients at the model's bottom, indicating the algorithm's enhanced stability and superior denoising performance. Subsequently, we also present the model increments of three algorithms at the thirtieth iteration. Since the optimization phase of FWI involves iterative cycling, the model increments at each iteration directly influence the inversion results. **Fig. 12(a)** illustrates the model increment for the Tikhonov regularization algorithm, where artefacts can be observed in the deep parts of the model, specifically within the 100m to 200m range.

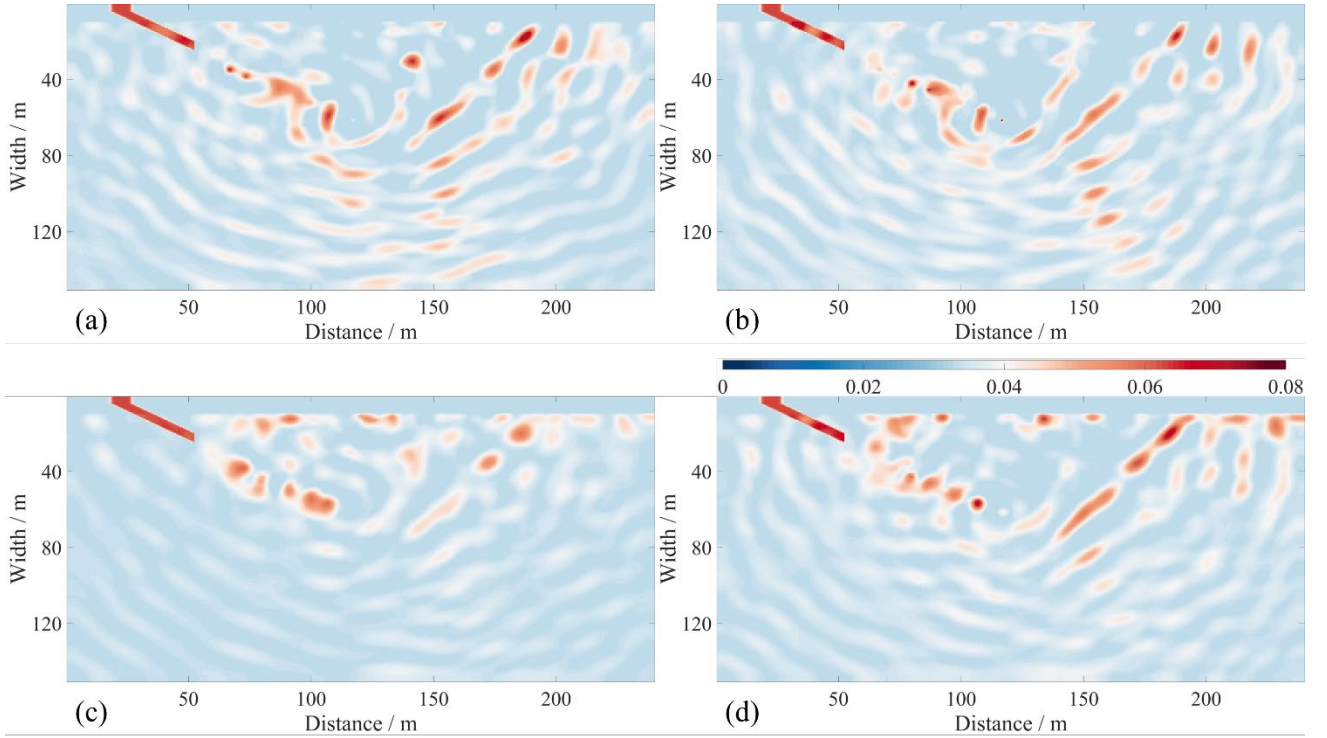


**Fig. 12.** Model increments at the 30th iteration. (a) Tikhonov regularization. (b) TV regularization. (c) Proposed modified FWI and  $\gamma = 1e-2$ . (d) Proposed modified FWI but  $\gamma = 1e-1$ .

These artefacts significantly reduce the interpretability of the inversion results, especially given their high amplitude, making it challenging to distinguish them from actual geological structures. **Fig. 12(b)** displays the model increment based on TV regularization, which shows fewer high-velocity artefacts, primarily concentrated after 150 meters. **Fig. 12(c)** shows the model increment at the 30th inversion iteration using the improved algorithm proposed at  $\gamma = 1e-2$  in this paper. **Fig. 12(c)** shows the model increment at the 30th inversion iteration using the improved algorithm proposed at  $\gamma = 1e-1$ . Notably, the improved algorithm results do not exhibit significant artefacts in the deeper parts of the model and provide higher accuracy in the inversion of faults and tunnels. This is attributed to the soft constrained objective function with a penalty term and a new convex optimization formulation proposed in this paper. Theoretically, in optimization problems like FWI,

the original problem can exhibit ill-conditioned behaviour due to its nonlinearity, leading to instability or imprecision in the solution process. For conventional constrained optimization problems, such as standard FWI, directly handling constraints can complicate the solution process, especially when the constraints are complex or nonlinear. Incorporating constraints through a penalty term into the objective function transforms a constrained problem into a soft-constrained one, thereby simplifying the solution process. This approach imposes a high cost on solutions that violate constraints, compelling the solver to find solutions that satisfy the constraints, and increase the condition number, thus improving the numerical stability and convergence of the solution process.

Finally, we present the comparisons of the one-dimensional velocity profiles from three different algorithms. **Fig. 13** compares the lateral velocities at 52 m (H-1) and 65 m (H-2) within the model, where the grey dashed line represents the initial model velocity curve, the black solid line is the benchmark velocity curve, the red solid line corresponds to the Tikhonov regularization-based velocity curve, the blue solid line is from the TV regularization FWI, the red solid line represents the improved algorithm at  $\gamma = 1e-2$  velocity curve, and the red solid line represents the improved algorithm at  $\gamma = 1e-1$  velocity curve.

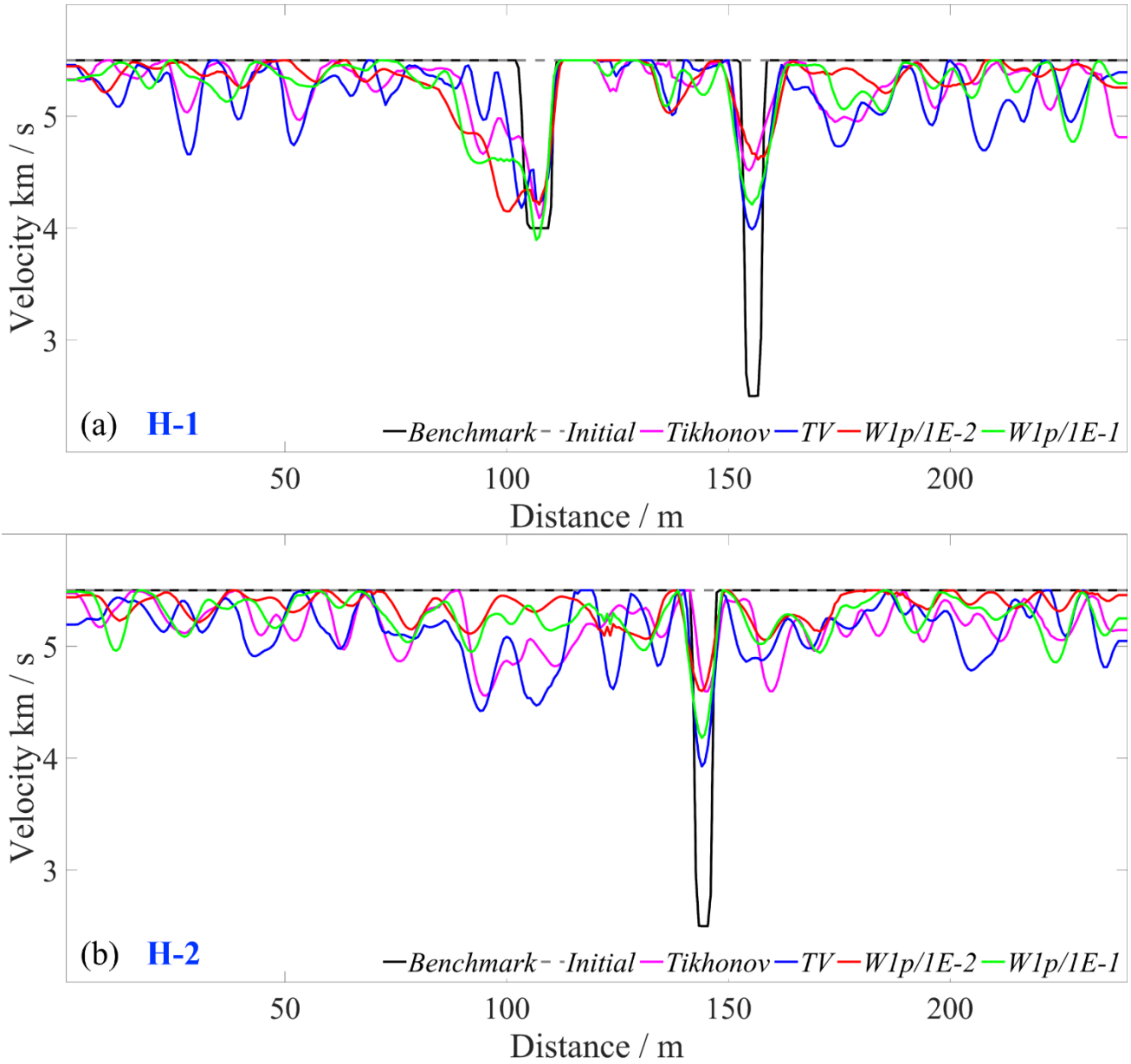


**Fig. 13.** Horizontal velocity profile analysis. (a) 52 m. (b) 65 m. The grey dotted line represents the initial velocity. The black dashed line represents the velocity of the benchmark; the magenta solid line represents the Tikhonov regularization FWI; the blue solid line represents the TV regularization FWI; the red solid line denotes the  $\gamma = 1e-2$  proposed modified FWI results velocity profile; the green solid line denotes the  $\gamma = 1e-1$  proposed modified FWI results velocity profile. The closer it approaches the black dashed line, the better the inversion results.



In **Fig. 13(a)**, a distinct tunnel velocity and another sharp velocity protrusion are observed, with other regions displaying unchanged velocity. It is evident that although the conventional algorithms can identify the location of structural bodies, their performance outside these structures is poor, particularly with sharp spikes and discontinuities at the model's two sides, indicating algorithmic instability. In contrast, the improved algorithm not only accurately identifies fault and tunnel locations but also demonstrates remarkable stability in the uniform velocity regions compared to the other two conventional algorithms. The conclusion of **Fig. 13(b)** is consistent with **Fig. 13(a)**. Additionally, **Fig. 14(a)** and **Fig. 14(b)** display the comparison of two sets of vertical velocity slices at 150 m (V-1) and 170 m (V-2) along the model's longitudinal axis.

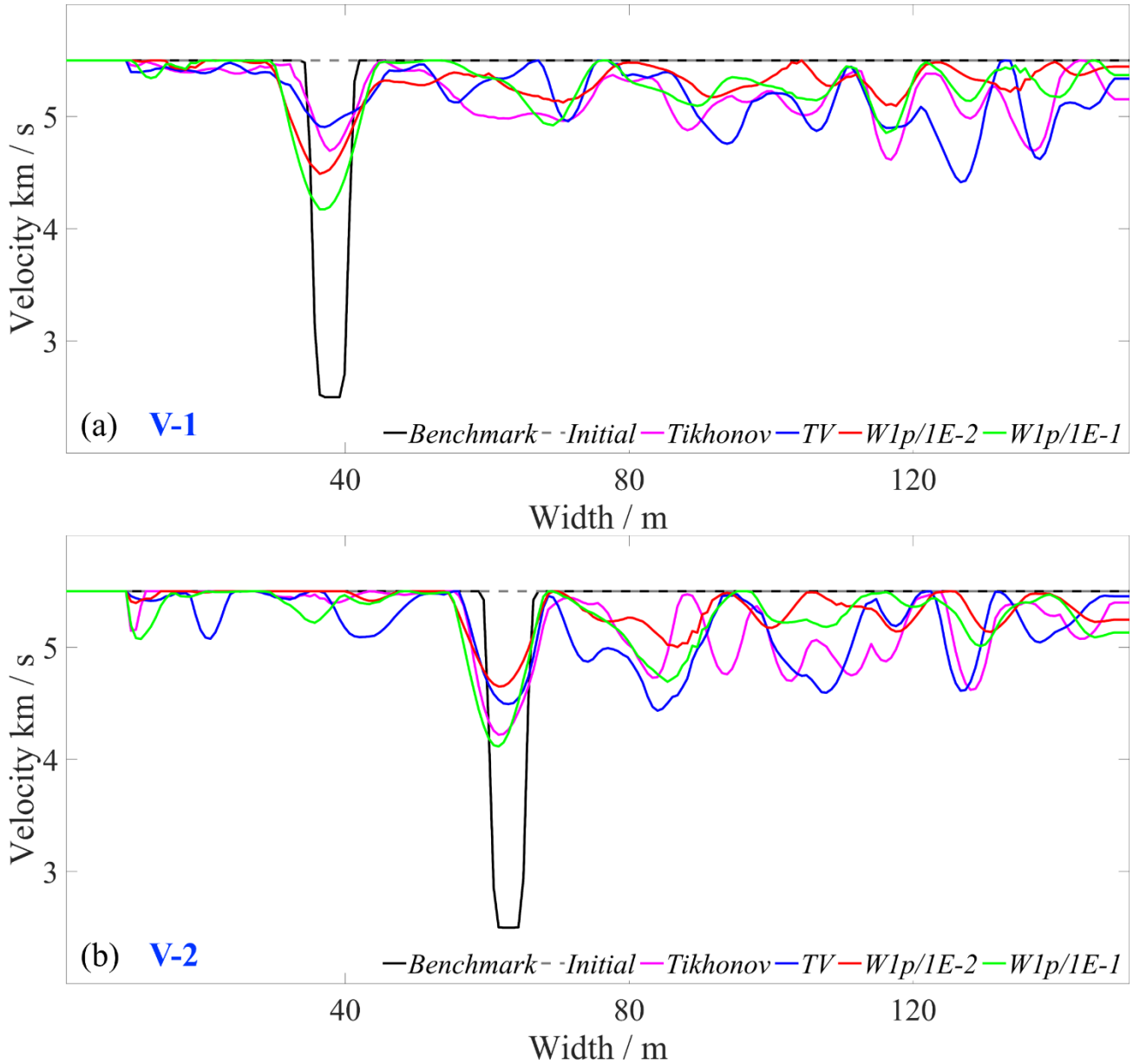


**Fig. 14.** Vertical velocity profile analysis. (a) 150 m. (b) 170 m. The grey dotted line represents the initial velocity. The black dashed line represents the velocity of the benchmark; the magenta solid line represents the Tikhonov regularization FWI; the blue solid line represents the TV regularization FWI; the red solid line denotes the  $\gamma = 1e-2$  proposed modified FWI results velocity profile; the green solid line denotes the  $\gamma = 1e-1$  proposed modified FWI results velocity profile. The closer it approaches the black dashed line, the better the inversion results.

Similar to the conclusions drawn from the previous figure, the proposed algorithm continues to demonstrate superior stability and interpretability. This is evident in its accurate fitting of fault structures and stable inversion of the surrounding rock velocities. Theoretically, by incorporating a quadratic penalty function, we expand the search space, and the optimal value obtained from the penalty function is always less than or equal to the original problem's optimal value, allowing us to interpret the penalty function as a relaxation of the original problem. This means that by introducing a penalty function into FWI, we can transform a constrained problem into a soft-constrained one. This not only simplifies the mathematical formulation and the solving process but also provides greater flexibility to adjust the intensity of the penalty terms, balancing the relationship between the objective function and constraint violations. This flexibility is particularly important as it allows us to tailor the model according to the characteristics of the data and the performance of the solving algorithm. In traditional FWI without a penalty function, the model may develop unrealistic physical properties (such as velocity anomalies) under conditions of poor data quality or incomplete data coverage. By incorporating penalty terms, the algorithm is compelled to avoid these non-physical solutions, enhancing the reliability and physical interpretability of the inversion results.

#### **4. Synthetic numerical simulation and inversion of two dual faults structure**

To further test the effectiveness, practicality and wide applicability of the algorithm proposed in this paper, we simulate and test the proposed algorithm in other two sets of models with double faults. Compared to a single-fault model structure, a dual faults scenario presents increased complexity in seismic wave interpretation. The transmission and refraction of seismic waves at the first fault result in very weak reflections at the second fault, with continuous energy attenuation. These weak reflection signals are difficult to identify in seismic records, thus complicating geological structure interpretation. Additionally, changes in wave velocity cause deviations in the wave propagation path. These deviations lead to discrepancies between the expected and actual positions of the second fault, resulting in identification errors. Consequently, recognizing dual faults structure is significantly more

challenging than single-fault structure, requiring higher algorithm stability and resolution.

#### 4.1. Test I: Double Thin Layer Fault Model

First, a model of a dual faults structure with the width of 5 m is constructed. As illustrated in **Fig. 15(a)**, the two faults are nearly parallel, each with a width of 5 m.

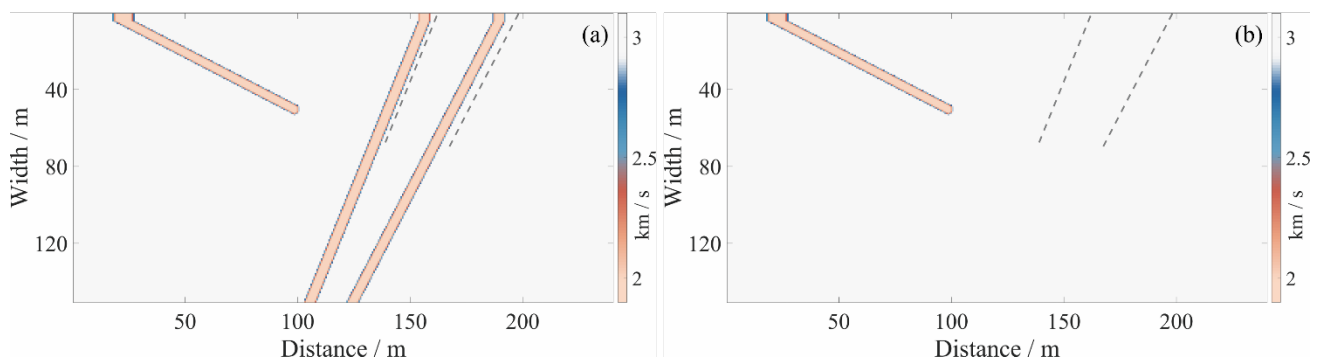


**Fig. 15.** Modelling of a dual faults structure for tunnel advance prediction. (a) Benchmark of the model with two tilted faults. (b) The initial model of the benchmark. The grey dotted lines indicate the location of the faults. All two faults have a width of 5 m.

The surrounding rock has a velocity of 3.0 km / s, while the faults have velocities of 2.0 km / s. The dip angles of the two faults are 65 degrees and 70 degrees, respectively. The top of this model is a non-free surface, and the overall dimensions of the model are 240 m in width and 140 m in depth. Additionally, a new acquisition system is designed for this model. Ten sources are placed at the tunnel face. Seven equally spaced receivers, numbered 1 to 7, are positioned at the tunnel bottom. Furthermore, 25 equally spaced receivers, numbered 8 to 32, are set up at the top of the model. **Fig. 15(b)** shows the initial velocity model. Given that the tunnel structure is known, the complete tunnel structure is included in this initial model. Subsequently, the wavefields for the sources and receivers are presented in **Fig. 16**. **Fig. 16(a)** shows the combined receiver data for receivers numbered 1-7 and

8-32. **Fig. 16(b)** illustrates the data with 4.9 dB random noise. **Fig. 16(c)** displays the noisy data.

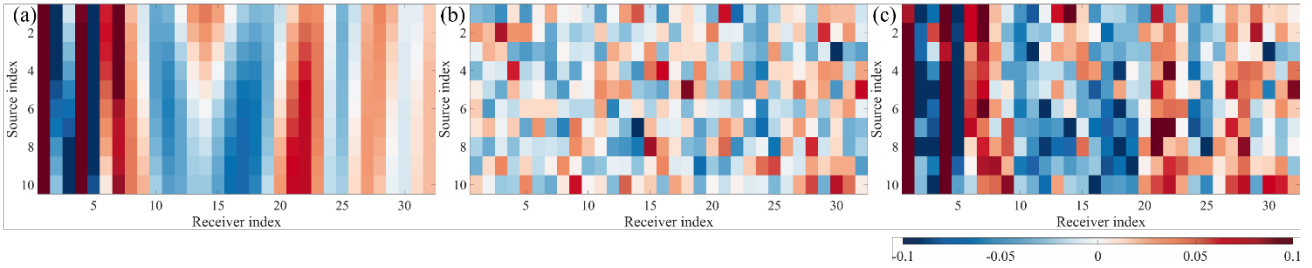


**Fig. 16.** Source receiver wavefield for the dual faults tunnel model. (a) The real part of the clean wavefield without noise component. The vertical coordinate explicit acquisition system consists of ten seismic sources, horizontal coordinates from 1 to 7 for receivers on the tunnel floor and from 8 to 32 for receivers on the free surface. (b) The real part of the random noise. (c) The real part of the wavefield with random noise as a means for further inversion.

In the FWI back-propagation calculation process, the quality of the scattered wavefield significantly affects the inversion results and convergence rate. A high-quality scattered wavefield can improve the accuracy of inversion results, accelerate convergence, and enhance the stability of the inversion process. **Fig. 17** illustrates the differences in the scattered wavefield between the improved algorithm and the conventional algorithm.

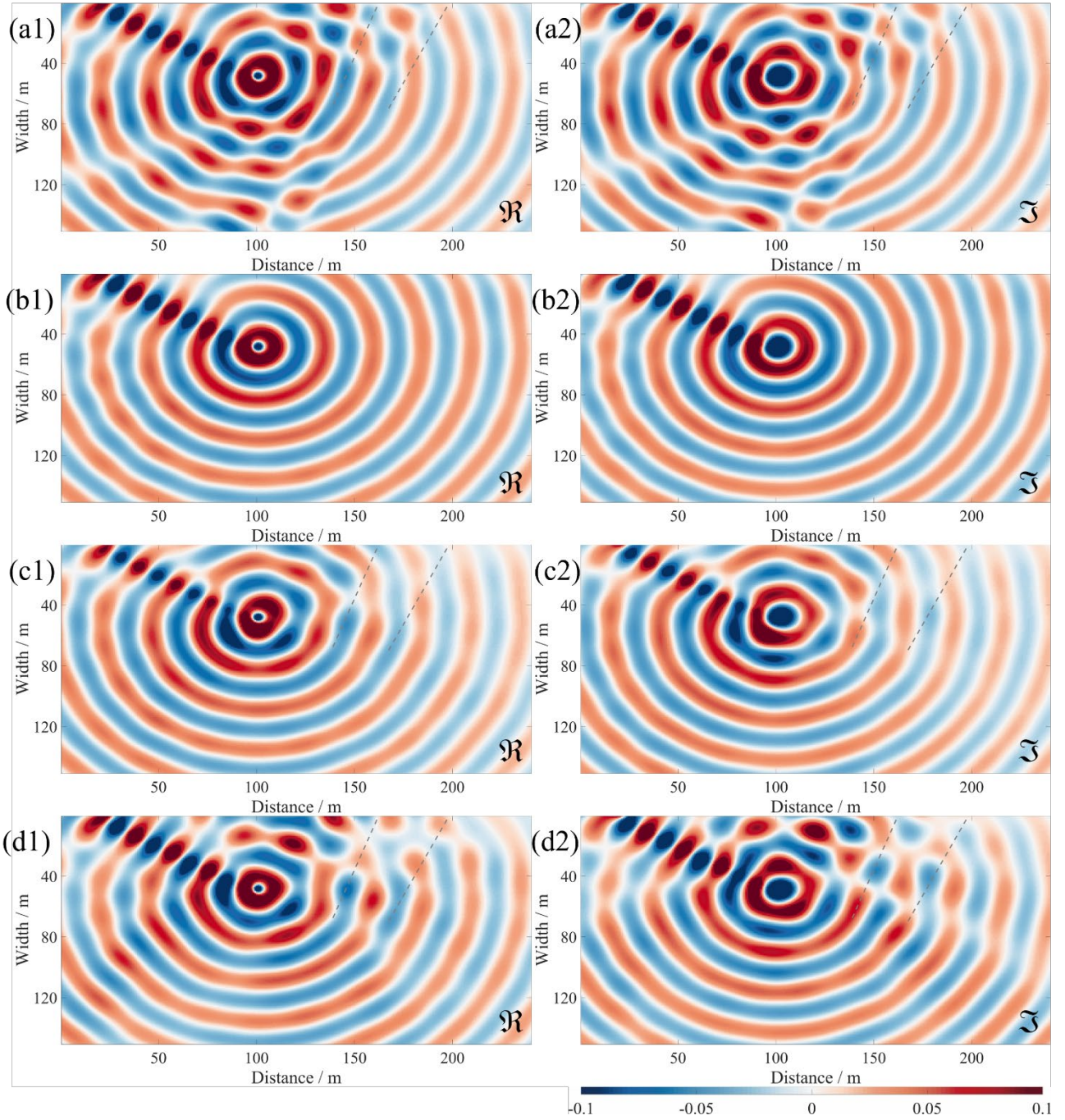


**Fig. 17.** The forward and background wavefields; and the scattered wavefields after the 1st iteration. (a1)-(a2) The real and imaginary part of the forward wavefield at 3.0 Hz. (b1)-(b2) The real and imaginary part of the background wavefield at 3.0 Hz. (c1)-(c2) The real and imaginary part of the scattered wavefield of LS method-based FWI at 3.0 Hz. (d1)-(d2) The real and imaginary part of the scattered wavefield of the quadratic penalty method-based FWI and  $\gamma = 1e-1$  at 3.0 Hz. The position of the grey auxiliary lines correspond to that in the true model.

Specifically, **Fig. 17(a1)-(a2)** show the forward wavefield of the true model at 3 Hz. **Fig. 17(b1)-(b2)** present the background wavefield obtained. **Fig. 17(c1)-(c2)** depict the scattered wavefield simulated by the conventional LS FWI after one iteration, whereas **Fig. 17(d1)-(d2)** display the scattered wavefield obtained using the improved algorithm. The scattered wavefield is used to compute the gradient, and the accuracy of the gradient directly affects the update of model parameters. Therefore, a high-quality scattered wavefield can provide more accurate gradient information, thereby improving the accuracy and convergence rate of the inversion results. Test results indicate that after one iteration, the improved algorithm's scattered wavefield can more rapidly capture model continuities structure, thus offering richer gradient information for the adjoint wavefield, leading to faster and more robust inversion.

Subsequently, we compared the true data corresponding to the 5th source with the simulated data from two algorithms, as illustrated in **Fig. 18**. **Fig. 18(a)** and **Fig. 18(b)** respectively show the real parts of the data comparisons for receivers numbered 1-7 and 8-32, while **Fig. 18(c)** and **Fig. 18(d)** present the corresponding imaginary parts.

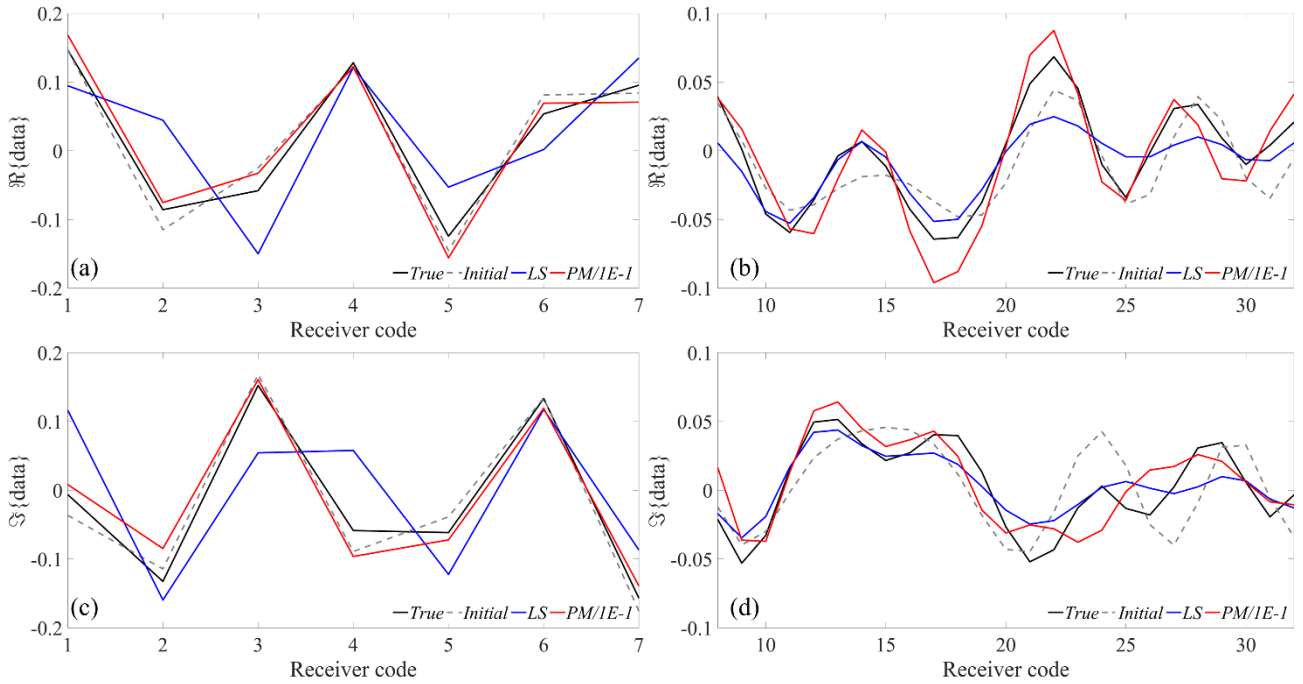


**Fig. 18.** Data for the 5th source and the 1st iteration. (a) The real part of the data received by receivers No.1-7. (b)



The real part of the data received by receivers No.8-32. (c) The imaginary part of the data received by receivers No.1-7. (d) The imaginary part of the data received by receivers No.8-32. Since the LS simulated data has a significant shift from the observed data, we consider its inversion to be difficult.

In the above figures, the black solid line represents the true data, the grey dashed line corresponds to the data from the initial model, the blue solid line denotes the simulated data after one iteration of the LS method, and the red solid line indicates the simulated data after one iteration of the proposed algorithm. The data after one iteration based on the LS method exhibits a significant shift compared to the observed data, indicating that subsequent inversions would be very challenging. In contrast, the simulated data from one iteration of the proposed algorithm closely matches the observed data and is not constrained by the initial model. This suggests that the improved algorithm, supported by an expanded search space, facilitates easier inversion and is less dependent on the initial model.

The inversion results of three algorithms are presented in **Fig. 19**. **Fig. 19(a1)-(a3)** show the inversion results based on Tikhonov regularization FWI, **Fig. 19(b1)-(b3)** depict TV regularization FWI's inversion results, and **Fig. 19(c1)-(c3)** illustrate the inversion results based on the proposed improved algorithm.



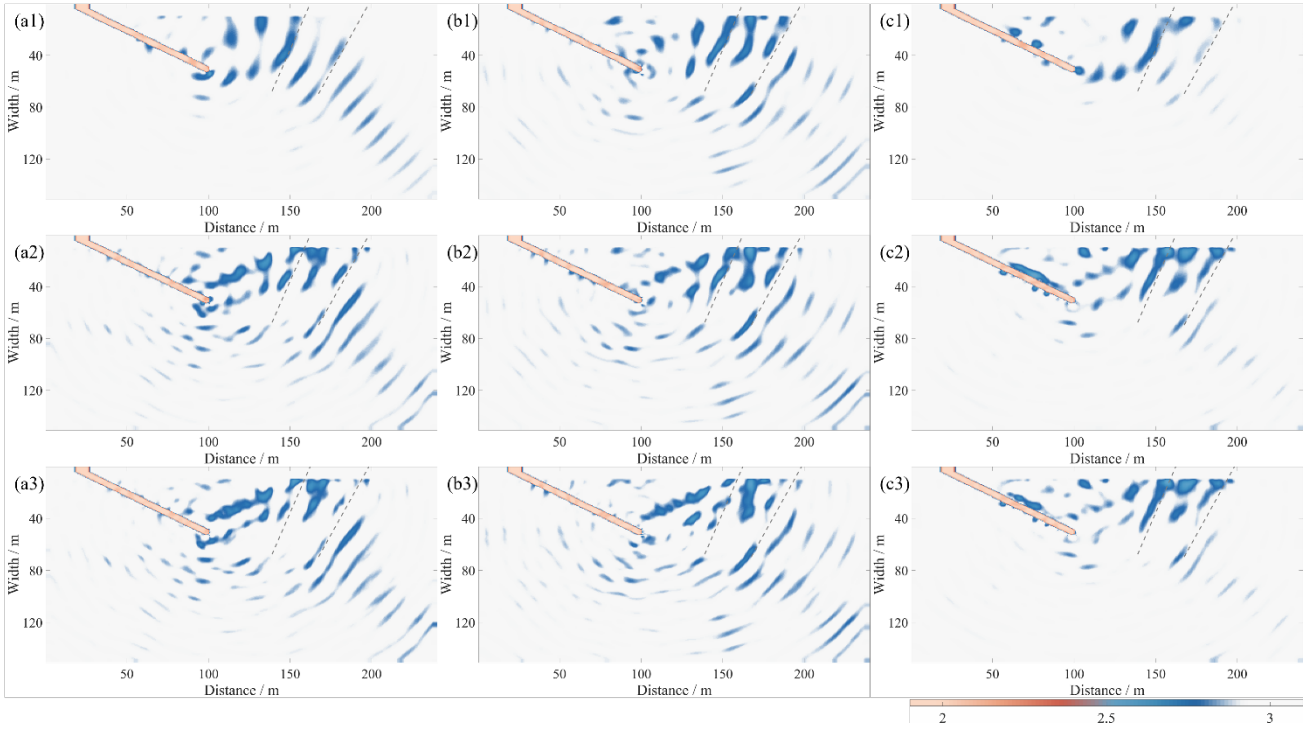


**Fig. 19.** Inversion results comparison. (a1)-(a3) Tikhonov-FWI regularization at 2.0 Hz, 3.5 Hz and 7.5 Hz. (b1)-(b3) TV-FWI in the same frequency range. (c1)-(c3) Proposed method in the same frequency range and  $\gamma = 1e - 1$ . The position of the grey auxiliary lines correspond to that in the true model.

The results indicate that the two conventional algorithms exhibit very blurred fault identification, and due to the significant influence of noise, distinguishing the target structure from artefacts is challenging. In contrast, the improved algorithm demonstrates better denoising capabilities. Compared to conventional algorithms, anomalies are less pronounced, and the simulating effect for the first fault is excellent. However, the inversion effect for the second fault is generally moderate due to reasons such as the shadowing effect of the first fault, which weakens the signal reflected from the second fault or causes it to be obscured by the reflection signal from the first fault. Although the improved algorithm shows certain enhancements over conventional algorithms for the second fault, there remains room for further improvement.

#### 4.2. Test II: Double Thick Layer Fault Model

Another topic of interest is the impact of fault thickness on the inversion results. For this purpose, we conducted Test II, as shown in **Fig. 20**. **Fig. 20(a)** presents the model for Test II, which is identical to the one used in Test I in terms of model data, source system and acquisition system, except for the adjustment of fault thickness from 5 m to 20 m, to investigate the effect of thick faults on FWI. **Fig. 20(b)** shows the initial model.

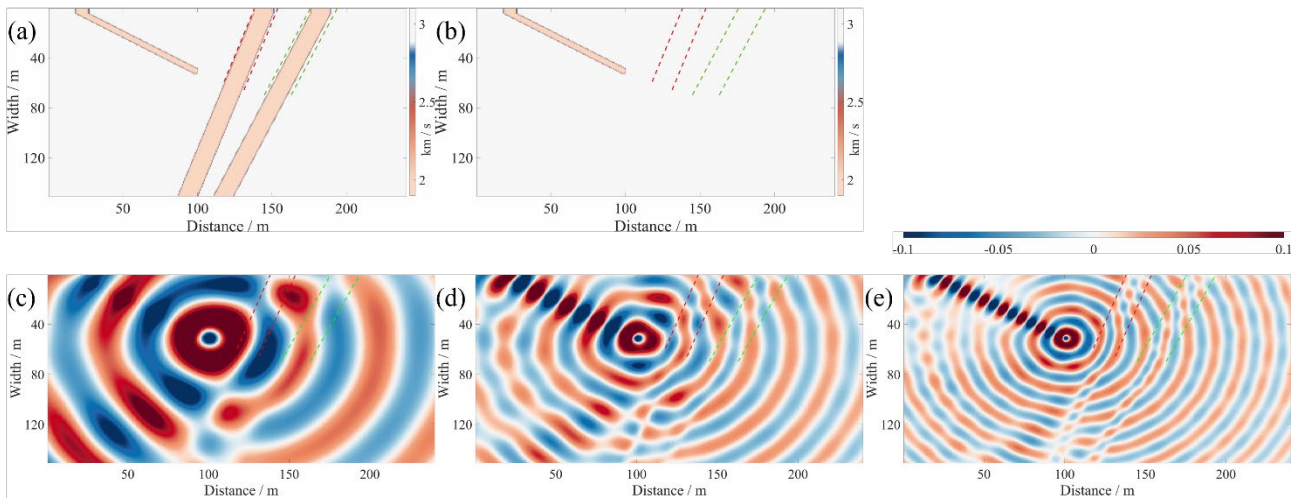


**Fig. 20.** A 20 m wide dual faults model. (a) True model (b) Initial model. (c) Forward wavefield at 1 Hz. (d) Forward wavefield at 2 Hz. (e) Forward wavefield at 3 Hz. The position of the coloured auxiliary lines correspond to that in the true model.

Given the changes in the target structures within the model, the source and acquisition systems need to be redesigned to address the challenges of this inversion according to the Nyquist sampling theorem and Fresnel zone theory. However, in this test, as the distance between the first reflection interface, second reflection interface and the source and receivers cannot be adjusted, the Fresnel zone formula suggests that only wavelength adjustments can address the inversion challenges. It is known that low frequencies, corresponding to long wavelengths, are more suitable for the inversion of large-scale structures, as they penetrate deeper and reduce the complexity of multipathing effects.

Additionally, the wavelength is proportional to the radius of the first Fresnel zone. Therefore, to tackle this inversion challenge, extremely low inversion frequencies were used to initiate the entire FWI process, as other conditions could not be altered. Different initial frequencies were tested to illustrate this scenario. **Fig. 20(c)** shows the forward modelling wavefield with a 1 Hz initial frequency, **Fig. 20(d)** with a 2 Hz initial frequency, and **Fig. 20(e)** with a 3 Hz initial frequency. The comparison reveals that the 1 Hz signal, with its longer wavelength and slower amplitude variation, can penetrate deeper structures, making it more suitable for the inversion of large-scale models. Consequently, in Test II, a multiscale inversion strategy was adopted, starting the inversion process from 1 Hz, with frequency intervals of 0.5 Hz.

Finally, a comparison of the inversion results from the two algorithms is presented in **Fig. 21**. **Fig. 21(a)-(d)** depict the inversion results based on Tikhonov regularization FWI, while **Fig. 21(e)-(h)** show the results from the improved algorithm proposed in this study.

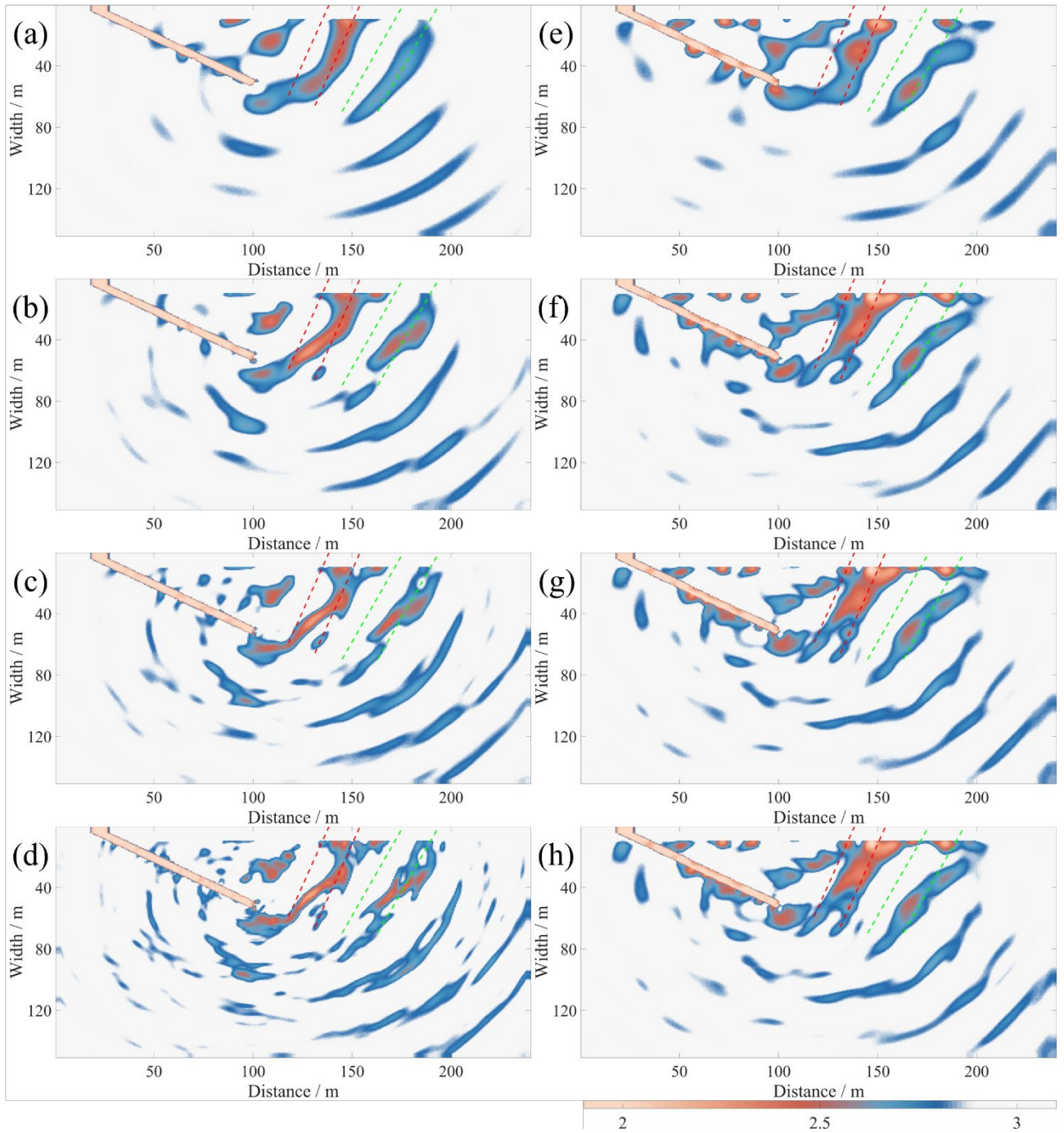


**Fig. 21.** Inversion results comparison. (a)-(d) Tikhonov-FWI regularization at 1.0 Hz, 2.0 Hz, 3.0 Hz and 4.0 Hz. (e)-(h) Proposed method in the same frequency range and  $\gamma = 1e-1$ . The position of the coloured auxiliary lines correspond to that in the true model.

The results indicate that both algorithms exhibit some fault location shifts, likely due to multipathing

effects. The anomalies observed at the receiver locations may be caused by multiple reflections from non-target reflectors. The comparison reveals that the conventional algorithm has poor fitting performance for thick faults. Although it can capture the general outline of the target structure at low frequencies, significant non-convergence issues arise with increased iterations. These issues may stem from the nonlinearity of the inversion problem and cycle skipping. Despite the improved algorithm still showing moderate performance in simulating the second fault, it achieves better simulation results for the first fault. The improved algorithm can generate a continuous anomalous velocity structure with clear boundaries, and the anomaly's location closely aligns with the true model. Therefore, the improved algorithm demonstrates significantly enhanced performance compared to the conventional algorithm.

## 5. Discussion

This paper introduced the use of an enhanced FWI algorithm for high-resolution inversion and imaging in advance prediction of tunnel constructions. FWI, originally developed for hydrocarbon exploration, has proven to be an effective and widely applicable inversion method in the resource exploration field. The fundamental theory and algorithmic framework of FWI also demonstrate its excellence as an inversion strategy, making it worthy of application in tunnel engineering projects. However, several specific issues need to be addressed and algorithmic improvements made to overcome particular challenges and difficulties, thereby accelerating the promotion and application of FWI in engineering problems.

Compared to large-scale, wide azimuth oil and gas exploration, especially in tunnel prediction problems, the data acquisition system can be significantly restricted, leading to incomplete seismic signal collection. Structures under tunnels, particularly those obscured by air cavities, often block the underlying structures, making weak P-wave reflection signals difficult to capture (Chen et al., [2021](#)), the same problem happens in the experiments of this paper. Therefore, it is necessary to design specific data acquisition systems tailored to particular geological structures to capture signal

responses in targeted areas. One of FWI's advantages is that it does not restrict the placement of sources and receivers to tunnel environments; configurations outside the tunnel are also acceptable, significantly enhancing flexibility, especially under small aperture conditions.

Furthermore, in the exploration and inversion of small-scale models for tunnel advance prediction, the role of high wavenumber signals requires greater consideration. At this time, the proposed FWI in this paper does not heavily depend on the initial model, nor does it rely extensively on low-frequency sampling, which is extremely beneficial for FWI. Although high wavenumber signals are sufficient to support FWI for tunnel advance prediction, this does not mean that low frequencies are entirely unnecessary (Bretaudeau et al., [2014](#)). Given that it is a nonlinear optimization problem, caution against local minima is still needed. Moreover, low-frequency waves have better penetration capabilities, allowing for the detection of deeper underground structures; therefore, adopting a multi-scale inversion strategy is necessary (Alani et al., [2020](#)).

Subsequently, considering that the LS method is sensitive to noise and outliers, it is necessary to consider a more robust sparse constraint (Farahmand et al., [2011](#)). Although an ideal state without any additional noise can achieve an ideal inversion result, in actual production, the noise issue is a critical and indispensable factor affecting the inversion results. This is also why strong noise was introduced in the tests conducted in this article. Conventional FWI algorithms, under large-scale conditions with the support of wide azimuth, multiple source blending, and other enhancements, can effectively improve the SNR (Krebs et al., [2009](#)). Additionally, in scenarios not emphasizing immediacy, conventional pre-processing of pre-stack data, such as filtering techniques and Radon transforms, can be used before proceeding with FWI (Feng, [2020](#)). However, there is not enough time to preprocess during the prediction of structures ahead of tunnel excavation, thus posing higher demands on FWI. Therefore, it is recommended to use enhanced techniques, firstly altering the optimization process and reconstructing the objective function to expand the search space and mitigate the issues caused by noise-induced local minima. Moreover, adopting more reasonable and flexible sparse constraints is also essential; beyond conventional TV regularization, it is advised to use more versatile regularization algorithms, including Huber regularization, K-support regularization, and a series of composite regularization algorithms to flexibly address noise issues (Li



et al., [2024a](#)).

Finally, considering that FWI is relatively expensive computationally compared to other commercialized methods such as TSP, the issue of computational cost still needs to be addressed. While transforming second-order optimization into first-order can reduce complexity, it also brings about slower convergence rates. Therefore, it is suggested to use more common optimization acceleration algorithms, such as the alternating direction method of multipliers (Aghamiry et al., [2022](#)).

In summary, after appropriately optimizing and improving FWI, it is very feasible and practical to apply it broadly and inexpensively in tunnel engineering projects.

## **6. Conclusion**

We attempt to apply an enhanced FWI based on a penalty method to the advance prediction of tunnel structures. Initially, in response to the limited space available in tunnel construction sites, a combined internal and external acquisition system is utilized, deploying only a few receivers inside the tunnel while placing the majority on the free surface above the tunnel. This combination provides a broader monitoring range and more comprehensive geological information, thereby enhancing the accuracy and timeliness of predictions. Further, research indicates that FWI, as a highly nonlinear optimization problem, exacerbates the high possibility of struggling in local minima with small-scale structures, making it particularly important and challenging to counteract local minima and cycle-skipping issues in tunnel advance prediction scenarios. Consequently, an improved FWI algorithm is proposed, incorporating the quadratic penalty techniques and the multi-scale inversion strategy. By utilizing convex relaxation techniques to transform hard constraints into soft constraints, the efficiency and flexibility of solving optimization problems are enhanced. The misfit function consists of two components: a data misfit term and a term driven by the wave equation, thus minimizing the model and wavefield to expand the search space, alleviating the nonlinearity of inversion and achieving high-resolution inversion. Experimental results also demonstrate that the

improved algorithm is not sensitive to the initial model. Subsequently, a Sobolev space regularization algorithm is specifically introduced to address potential random noise issues during engineering exploration. By adjusting different regularization parameters based on noise amplitude, data characteristics, and model features, the regularization path is flexibly adjusted. Lastly, the proposed improved system is applied to some classical fault tunnel advance prediction models. The improved algorithm is also compared and discussed against two other conventional algorithms, with test results validating the effectiveness and superiority of the proposed algorithm. Both theoretical and experimental evidence confirm that applying FWI to tunnel advance prediction is highly feasible and accurate.

## **Declaration of competing interest**

The authors declare that they have no known competing financial interests or personal relationships that could have appeared to influence the work reported in this paper.

## **Data availability**

Data associated with this research are confidential and cannot be released.

## **Acknowledgements**

1. This work was supported by the XXXX [grant numbers xxxx, yyyy]; the XXXXXXXX [grant number zzzz]; and the XXXXX [grant number aaaa].

2. This research did not receive any specific grant from funding agencies in the public, commercial, or not-for-profit sectors.



## Appendix A. From Least Square to Lagrangian Multipliers to Penalty Method & Parameter Stability

In this appendix, we elaborate in detail on how to calculate the misfit and gradient update based on the penalty method. The objective of the optimisation process for FWI is to compute the minimum value of the misfit function (Leeuwen and Herrmann, [2015](#)):

$$\min_{\mathbf{m}, \mathbf{u}} f(\mathbf{m}), \quad (\text{A.1})$$

classic algorithms include the explicit imposition of constraints on the objective function:

$$\min_{\mathbf{m}, \mathbf{u}} \|\mathbf{P}\mathbf{u} - \mathbf{D}\|_2^2 \quad \text{s.t.} \quad \mathbf{A}(\mathbf{m})\mathbf{u} = \mathbf{S}, \quad (\text{A.2})$$

at this point, the objective function is described as follows:

$$f(\mathbf{m}) = \|\mathbf{D} - \mathbf{P}\mathbf{A}(\mathbf{m})^{-1}\mathbf{S}\|_2^2, \quad (\text{A.3})$$

a well-known weakness of classic algorithms is their propensity to fall into local minima. Consequently, a full-space algorithm has been proposed, related to the saddle-point problem of the Lagrange method:

$$\max_{\mathbf{v}} \min_{\mathbf{m}, \mathbf{u}} \mathcal{L}(\mathbf{m}, \mathbf{u}, \mathbf{v}), \quad (\text{A.4})$$

here,  $\mathbf{v}$  is a linear space of the same dimension as the wavefield space:

$$\mathcal{L}(\mathbf{m}, \mathbf{u}, \mathbf{v}) = \|\mathbf{P}\mathbf{u} - \mathbf{D}\|_2^2 + \langle \mathbf{v}, \mathbf{A}(\mathbf{m})\mathbf{u} - \mathbf{S} \rangle, \quad (\text{A.5})$$

the method of Lagrangian multipliers optimizes jointly over the model parameters, wavefield, and  $\mathbf{v}$ . Due to the sparsity of the Hessian matrix in Lagrangian, it is theoretically feasible to advance gradient optimization to the second order:

$$\nabla \mathcal{L}(\mathbf{m}, \mathbf{u}, \mathbf{v}) = \begin{pmatrix} \mathcal{L}_{\mathbf{m}} \\ \mathcal{L}_{\mathbf{u}} \\ \mathcal{L}_{\mathbf{v}} \end{pmatrix} = \begin{pmatrix} \mathbf{G}(\mathbf{m}, \mathbf{u})^T \mathbf{v} \\ \mathbf{A}(\mathbf{m})^T \mathbf{v} + \mathbf{P}^T (\mathbf{P}\mathbf{u} - \mathbf{D}) \\ \mathbf{A}(\mathbf{m})\mathbf{u} - \mathbf{S} \end{pmatrix}, \quad (\text{A.6})$$

and:

$$\nabla^2 \mathcal{L}(\mathbf{m}, \mathbf{u}, \mathbf{v}) = \begin{pmatrix} \mathbf{R}(\mathbf{m}, \mathbf{u}, \mathbf{v}) & \mathbf{K}(\mathbf{m}, \mathbf{v})^T & \mathbf{G}(\mathbf{m}, \mathbf{u})^T \\ \mathbf{K}(\mathbf{m}, \mathbf{v}) & \mathbf{P}^T \mathbf{P} & \mathbf{A}(\mathbf{m})^T \\ \mathbf{G}(\mathbf{m}, \mathbf{u}) & \mathbf{A}(\mathbf{m}) & 0 \end{pmatrix}, \quad (\text{A.7})$$

where:

$$\mathbf{G}(\mathbf{m}, \mathbf{u}) = \frac{\partial \mathbf{A}(\mathbf{m})\mathbf{u}}{\partial \mathbf{m}}, \quad \mathbf{K}(\mathbf{m}, \mathbf{v}) = \frac{\partial \mathbf{A}(\mathbf{m})^T \mathbf{v}}{\partial \mathbf{m}}, \quad \mathbf{R}(\mathbf{m}, \mathbf{u}, \mathbf{v}) = \frac{\partial \mathbf{G}(\mathbf{m}, \mathbf{u})^T \mathbf{v}}{\partial \mathbf{m}}, \quad (\text{A.8})$$

when  $\mathbf{A}$  is sparse, these Jacobian matrices are usually sparse and can be analytically computed.

However, the major issue with this algorithm is the considerable difficulty in storing  $\mathbf{v}$  in memory, which demands high requirements. Therefore, a simplified version of half-space optimization has been proposed:

$$\min_{\mathbf{m}, \mathbf{u}} F(\mathbf{m}) = \min_{\mathbf{m}, \mathbf{u}} \|\mathbf{P}\mathbf{u} - \mathbf{D}\|_2^2 + \tau \|\mathbf{A}(\mathbf{m})\mathbf{u} - \mathbf{S}\|_2^2, \quad (\text{A.9})$$

where  $\mathbf{u}$  is the solution to the quadratic penalty equation:

$$\begin{pmatrix} \mathbf{P} \\ \tau \mathbf{A}(\mathbf{m}) \end{pmatrix} \mathbf{u} = \begin{pmatrix} \mathbf{D} \\ \tau \mathbf{S} \end{pmatrix}, \quad (\text{A.10})$$

then:

$$(\mathbf{P}^H \mathbf{P} + \tau^2 \mathbf{A}(\mathbf{m})^H \mathbf{A}(\mathbf{m})) \mathbf{u} = \mathbf{P}^H \mathbf{D} + \tau^2 \mathbf{A}(\mathbf{m})^H \mathbf{S}, \quad (\text{A.11})$$

compared to the method of Lagrangian multipliers, the gradient optimization process of the simplified version is easier, and the second order does not involve the  $\mathbf{v}$  component:

$$\nabla F = \begin{pmatrix} F_{\mathbf{m}} \\ F_{\mathbf{u}} \end{pmatrix} = \begin{pmatrix} \tau \mathbf{G}(\mathbf{m}, \mathbf{u})^T (\mathbf{A}(\mathbf{m})\mathbf{u} - \mathbf{S}) \\ \mathbf{P}^T (\mathbf{P}\mathbf{u} - \mathbf{D}) + \tau \mathbf{A}(\mathbf{m})^T (\mathbf{A}(\mathbf{m})\mathbf{u} - \mathbf{S}) \end{pmatrix}, \quad (\text{A.12})$$

and:

$$\nabla^2 F = \begin{pmatrix} F_{\mathbf{m},\mathbf{m}} & F_{\mathbf{m},\mathbf{u}} \\ F_{\mathbf{u},\mathbf{m}} & F_{\mathbf{u},\mathbf{u}} \end{pmatrix}, \quad (\text{A.13})$$

where:

$$F_{\mathbf{m},\mathbf{m}} = \tau (\mathbf{G}(\mathbf{m}, \mathbf{u})^T \mathbf{G}(\mathbf{m}, \mathbf{u}) + \mathbf{R}(\mathbf{m}, \mathbf{u}, \mathbf{A}(\mathbf{m})\mathbf{u} - \mathbf{S})), \quad (\text{A.14})$$

$$F_{\mathbf{m},\mathbf{u}} = \tau (\mathbf{K}(\mathbf{m}, \mathbf{A}(\mathbf{m})\mathbf{u} - \mathbf{S}) + \mathbf{A}(\mathbf{m})^T \mathbf{G}(\mathbf{m}, \mathbf{u})), \quad (\text{A.15})$$

$$F_{\mathbf{u},\mathbf{u}} = \mathbf{P}^T \mathbf{P} + \tau \mathbf{A}(\mathbf{m})^T \mathbf{A}(\mathbf{m}), \quad (\text{A.16})$$

we introduce:

$$\mathbf{u}_\tau(\mathbf{m}) = \arg \min_{\mathbf{u}} F(\mathbf{m}, \mathbf{u}), \quad (\text{A.17})$$

and define:

$$\Phi(\mathbf{m}) = F(\mathbf{m}, \mathbf{u}_\tau(\mathbf{m})), \quad (\text{A.18})$$

from this, we can derive the closed-form solution of the optimization problem:

$$\mathbf{u}_\tau = (\tau \mathbf{A}^T(\mathbf{m})\mathbf{A}(\mathbf{m}) + \mathbf{P}^T \mathbf{P})^{-1} (\tau \mathbf{A}^T(\mathbf{m})\mathbf{S} + \mathbf{P}\mathbf{D}), \quad (\text{A.19})$$

the above equation corresponds to Eq. (6). And we can get:

$$\mathbf{v}_\tau = \tau (\mathbf{A}\mathbf{u}_\tau - \mathbf{S}), \quad (\text{A.20})$$

Moreover, according to Eq. (A.7), we can obtain the gradient expression of the Lagrangian function with soft constraints

$$\begin{pmatrix} \mathbf{R}(\mathbf{m}, \mathbf{u}, \mathbf{v}) & \mathbf{K}(\mathbf{m}, \mathbf{v})^T & \mathbf{G}(\mathbf{m}, \mathbf{u})^T \\ \mathbf{K}(\mathbf{m}, \mathbf{v}) & \mathbf{P}^T \mathbf{P} & \mathbf{A}(\mathbf{m})^T \\ \mathbf{G}(\mathbf{m}, \mathbf{u}) & \mathbf{A}(\mathbf{m}) & 0 \end{pmatrix} \begin{pmatrix} \mathbf{m}_\tau^* - \mathbf{m}^* \\ \mathbf{u}_\tau^* - \mathbf{u}^* \\ \mathbf{v}_\tau^* - \mathbf{v}^* \end{pmatrix} = \begin{pmatrix} \mathcal{L}_m(\mathbf{m}_\tau^*, \mathbf{u}_\tau^*, \mathbf{v}_\tau^*) \\ 0 \\ \tau^{-1} \mathbf{v}^* + \mathcal{O}(\tau^{-2}) \end{pmatrix}, \quad (\text{A.21})$$

we find:

$$\begin{aligned} & (\mathbf{R} - \mathbf{K}^T \mathbf{A}^{-1} \mathbf{G} - \mathbf{G}^T \mathbf{A}^{-T} \mathbf{K} + \mathbf{G}^T \mathbf{A}^{-T} \mathbf{P}^T \mathbf{P} \mathbf{A}^{-1} \mathbf{G})(\mathbf{m}_\tau^* - \mathbf{m}^*) = \\ & \mathcal{L}_m(\mathbf{m}_\tau^*, \mathbf{u}_\tau^*, \mathbf{v}_\tau^*) + \tau^{-1} \mathbf{Q} \mathbf{v}^* + \mathcal{O}(\tau^{-2}), \end{aligned} \quad (\text{A.22})$$

where:

$$\mathbf{Q} = \mathbf{G}^T \mathbf{A}^{-T} \mathbf{P}^T \mathbf{P} \mathbf{A}^{-1} - \mathbf{K}^T \mathbf{A}^{-1}, \quad (\text{A.23})$$

then, after ignoring the second-order term of the reduced Hessian matrix, we get:

$$\mathbf{H} \approx \mathbf{G}^T \mathbf{A}^{-T} \mathbf{P}^T \mathbf{P} \mathbf{A}^{-1} \mathbf{G}, \quad (\text{A.24})$$

and:

$$\mathbf{Q} \approx \mathbf{G}^T \mathbf{A}^{-T} \mathbf{P}^T \mathbf{P} \mathbf{A}^{-1}, \quad (\text{A.25})$$

then, we can find

$$\|\mathbf{m}_\tau^* - \mathbf{m}^*\|_2 \leq \|\mathbf{H}^{-1}\|_2 (\varepsilon + \tilde{\tau}^{-1} \|\mathbf{G}^T \mathbf{A}^{-T} \mathbf{P}^T\|_2 \|\mathbf{D} - \mathbf{P} \mathbf{A}(\mathbf{m}_\tau^*)^{-1} \mathbf{S}\|_2), \quad (\text{A.26})$$

where:

$$\mu = \|\mathbf{D} - \mathbf{P} \mathbf{A}(\mathbf{m}_\tau^*)^{-1} \mathbf{S}\|_2, \quad (\text{A.27})$$

represents the data mismatch. The subsequent priority is to introduce the scaling operation

$$\|\mathbf{m}_\tau^* - \mathbf{m}^*\|_2 \leq \|\mathbf{H}^{-1}\|_2 (\tilde{\varepsilon} + \tilde{\tau}^{-1} \tilde{\mu}), \quad (\text{A.28})$$

based on this, we reconstruct partial model parameters using the principal eigenvectors, rather than a complete reconstruction. We discuss the different scaling levels in detail in the experimental section.

## References

- Abdoulav, G.S., Ren, K., Hielscher, A.H., 2005. Optical tomography as a PDE-constrained optimization problem. *Inverse Problems* 21, 1507. <https://doi.org/10.1088/0266-5611/21/5/002>
- Adams, R.A., Fournier, J.J.F., 2003. Sobolev spaces. Elsevier.
- Aghamiry, H.S., Gholami, A., Operto, S., Malcolm, A., 2022. ADMM-based full-waveform inversion for microseismic imaging. *Geophysical Journal International* 228, 259–274. <https://doi.org/10.1093/gji/ggab332>
- Aghazade, K., Gholami, A., Aghamiry, H.S., Operto, S., 2022. Anderson-accelerated augmented lagrangian for extended waveform inversion. *Geophysics* 87, R79–R91. <https://doi.org/10.1190/geo2021-0409.1>
- Alani, A.M., Tosti, F., Ciampoli, L.B., Gagliardi, V., Benedetto, A., 2020. An integrated investigative approach in health monitoring of masonry arch bridges using GPR and InSAR technologies. *NDT & E International, Data Fusion, Integration and Advances of Non-Destructive Testing Methods in Civil and Environmental Engineering* 115, 102288. <https://doi.org/10.1016/j.ndteint.2020.102288>
- Ashida, Y., 2001. Seismic imaging ahead of a tunnel face with three-component geophones. *International Journal of Rock Mechanics and Mining Sciences, Application of Geophysics to Rock Engineering* 38, 823–831. [https://doi.org/10.1016/S1365-1609\(01\)00047-8](https://doi.org/10.1016/S1365-1609(01)00047-8)
- Asnaashari, A., Brossier, R., Garambois, S., Audebert, F., Thore, P., Virieux, J., 2013. Regularized seismic full waveform inversion with prior model information. *Geophysics* 78, R25–R36. <https://doi.org/10.1190/geo2012-0104.1>
- Athanasopoulos, G.A., Pelekis, P.C., 2000. Ground vibrations from sheetpile driving in urban environment: measurements, analysis and effects on buildings and occupants. *Soil Dynamics and Earthquake Engineering* 19, 371–387. [https://doi.org/10.1016/S0267-7261\(00\)00008-7](https://doi.org/10.1016/S0267-7261(00)00008-7)
- Banerjee, B., Walsh, T.F., Aquino, W., Bonnet, M., 2013. Large scale parameter estimation problems in frequency-domain elastodynamics using an error in constitutive equation functional. *Computer Methods in Applied Mechanics and Engineering* 253, 60–72. <https://doi.org/10.1016/j.cma.2012.08.023>
- Bharadwaj, P., Drijkoningen, G., Mulder, W., Thorbecke, J., Neduzca, B., Jenneskens, R., 2017. A shear-wave seismic system using full-waveform inversion to look ahead of a tunnel-boring machine. *Near Surface Geophysics* 15, 210–225. <https://doi.org/10.3997/1873-0604.2017014>
- Biondi, E., Barnier, G., Clapp, R.G., Picetti, F., Farris, S., 2021. An object-oriented optimization framework for large-scale inverse problems. *Computers & Geosciences* 154, 104790. <https://doi.org/10.1016/j.cageo.2021.104790>
- Brandsberg-Dahl, S., Chemingui, N., Valenciano, A., Ramos-Martinez, J., Qiu, L., 2017. FWI for model updates in large-contrast media. *the Leading Edge* 36, 81–87. <https://doi.org/10.1190/tle36010081.1>
- Bretaudeau, F., Gélis, C., Leparoux, D., Brossier, R., Cabrera, J., Côte, P., 2014. High-resolution quantitative seismic imaging of a strike-slip fault with small vertical offset in clay rocks from underground galleries: experimental platform of tournemire, france. *Geophysics* 79, B1–B18. <https://doi.org/10.1190/geo2013-0082.1>
- Brossier, R., Operto, S., Virieux, J., 2009. Seismic imaging of complex onshore structures by 2D elastic frequency-domain full-waveform inversion. *Geophysics* 74, WCC105–WCC118. <https://doi.org/10.1190/1.3215771>
- Chen, H., Nie, X., Gan, S., Zhao, Y., Qiu, H., 2021. Interfacial imperfection detection for steel-concrete composite structures using NDT techniques: a state-of-the-art review. *Engineering Structures* 245, 112778. <https://doi.org/10.1016/j.engstruct.2021.112778>
- Cheng, F., Liu, J., Qu, N., Mao, M., Zhou, L., 2014. Two-dimensional pre-stack reverse time imaging based on tunnel space. *Journal of Applied Geophysics* 104, 106–113. <https://doi.org/10.1016/j.jappgeo.2014.02.013>

- Chowdhery, A., Narang, S., Devlin, J., Bosma, M., Mishra, G., Roberts, A., Barham, P., Chung, H.W., Sutton, C., Gehrmann, S., Schuh, P., Shi, K., Tsvyashchenko, S., Maynez, J., Rao, A., Barnes, P., Tay, Y., Shazeer, N., Prabhakaran, V., Reif, E., Du, N., Hutchinson, B., Pope, R., Bradbury, J., Austin, J., Isard, M., Gur-Ari, G., Yin, P., Duke, T., Levskaya, A., Ghemawat, S., Dev, S., Michalewski, H., Garcia, X., Misra, V., Robinson, K., Fedus, L., Zhou, D., Ippolito, D., Luan, D., Lim, H., Zoph, B., Spiridonov, A., Sepassi, R., Dohan, D., Agrawal, S., Omernick, M., Dai, A.M., Pillai, T.S., Pellat, M., Lewkowycz, A., Moreira, E., Child, R., Polozov, O., Lee, K., Zhou, Z., Wang, X., Saeta, B., Diaz, M., Firat, O., Catasta, M., Wei, J., Meier-Hellstern, K., Eck, D., Dean, J., Petrov, S., Fiedel, N., 2023. PaLM: Scaling Language Modeling with Pathways. *Journal of Machine Learning Research* 24, 1–113.
- Farahmand, S., Giannakis, G.B., Angelosante, D., 2011. Doubly robust smoothing of dynamical processes via outlier sparsity constraints. *IEEE Trans. Signal Process.* 59, 4529–4543. <https://doi.org/10.1109/TSP.2011.2161300>
- Feng, D., Ding, S., Wang, Xun, Wang, Xiangyu, 2022. Wavefield reconstruction inversion of GPR data for permittivity and conductivity models in the frequency domain based on modified total variation regularization. *Ieee Transactions on Geoscience and Remote Sensing* 60, 1–14. <https://doi.org/10.1109/TGRS.2021.3077476>
- Feng, R., 2020. Estimation of reservoir porosity based on seismic inversion results using deep learning methods. *Journal of Natural Gas Science and Engineering* 77, 103270. <https://doi.org/10.1016/j.jngse.2020.103270>
- Fischer, S., Steinwart, I., 2020. Sobolev norm learning rates for regularized least-squares algorithms. *Journal of Machine Learning Research* 21, 1–38.
- Francese, R.G., Hajnal, Z., Prugger, A., 2002. High-resolution images of shallow aquifers—a challenge in near-surface seismology. *Geophysics* 67, 177–187. <https://doi.org/10.1190/1.1451490>
- Gholami, A., Aghamiry, H.S., Operto, S., 2022. Extended-space full-waveform inversion in the time domain with the augmented lagrangian method. *Geophysics* 87, R63–R77. <https://doi.org/10.1190/geo2021-0186.1>
- Gholami, A., Aghazade, K., 2024. Full waveform inversion and lagrange multipliers. *Geophysical Journal International* ggae148. <https://doi.org/10.1093/gji/ggae148>
- Grote, M.J., Huber, J., Kourounis, D., Schenk, O., 2014. Inexact interior-point method for PDE-constrained nonlinear optimization. *SIAM J. Sci. Comput.* 36, A1251–A1276. <https://doi.org/10.1137/130921283>
- Habashy, T.M., Abubakar, A., Pan, G., Belani, A., 2011. Source-receiver compression scheme for full-waveform seismic inversion. *Geophysics* 76, R95–R108. <https://doi.org/10.1190/1.3590213>
- Hanson, D.R., Vandergrift, T.L., DeMarco, M.J., Hanna, K., 2002. Advanced techniques in site characterization and mining hazard detection for the underground coal industry. *International Journal of Coal Geology*, Volume 50 50, 275–301. [https://doi.org/10.1016/S0166-5162\(02\)00121-0](https://doi.org/10.1016/S0166-5162(02)00121-0)
- Huang, G., Nammour, R., Symes, W., 2017. Full-waveform inversion via source-receiver extension. *Geophysics* 82, R153–R171. <https://doi.org/10.1190/geo2016-0301.1>
- Inazaki, T., Isahai, H., Kawamura, S., Kurahashi, T., Hayashi, H., 1999. Stepwise application of horizontal seismic profiling for tunnel prediction ahead of the face. *the Leading Edge* 18, 1429–1431. <https://doi.org/10.1190/1.1438246>
- Kazci, V.V., Kalita, M., Alkhalifah, T., 2017. Salt-body inversion with minimum gradient support and sobolev space norm regularizations. Presented at the 79th EAGE Conference and Exhibition 2017, European Association of Geoscientists & Engineers, pp. 1–5. <https://doi.org/10.3997/2214-4609.201700600>
- Klotzsche, A., Vereecken, H., van der Kruk, J., 2019. Review of crosshole ground-penetrating radar full-waveform inversion of experimental data: recent developments, challenges, and pitfalls. *Geophysics* 84, H13–H28. <https://doi.org/10.1190/geo2018-0597.1>
- Krebs, J.R., Anderson, J.E., Hinkley, D., Neelamani, R., Lee, S., Baumstein, A., Lacasse, M.-D., 2009. Fast full-wavefield seismic inversion using encoded sources. *Geophysics* 74, WCC177–WCC188. <https://doi.org/10.1190/1.3230502>

- Leeuwen, T. van, Herrmann, F.J., 2015. A penalty method for PDE-constrained optimization in inverse problems. *Inverse Problems* 32, 015007. <https://doi.org/10.1088/0266-5611/32/1/015007>
- Li, J., Mikada, H., Takekawa, J., 2024a. Improved full-waveform inversion for seismic data in the presence of noise based on the K-support norm. *Pure Appl. Geophys.*, 1-28. <https://doi.org/10.1007/s00024-024-03449-5>
- Li, J., Mikada, H., Takekawa, J., 2024b. Inexact augmented lagrangian method-based full-waveform inversion with randomized singular value decomposition. *Journal of Geophysics and Engineering* 21, 572–597. <https://doi.org/10.1093/jge/gxae015>
- Li, S., Liu, B., Xu, X., Nie, L., Liu, Z., Song, J., Sun, H., Chen, L., Fan, K., 2017. An overview of ahead geological prospecting in tunneling. *Tunnelling and Underground Space Technology* 63, 69–94. <https://doi.org/10.1016/j.tust.2016.12.011>
- Liu, B., Gong, Z., Zhang, F., Xu, X., Zhao, Y., Chen, L., 2023. Full-waveform inversion method for tunnel seismic forward prospecting. *Geophysical Journal International* 232, 2186–2204. <https://doi.org/10.1093/gji/ggac375>
- Liu, D.C., Nocedal, J., 1989. On the limited memory BFGS method for large scale optimization. *Mathematical Programming* 45, 503–528. <https://doi.org/10.1007/BF01589116>
- Métivier, L., Brossier, R., Mérigot, Q., Oudet, E., Virieux, J., 2016. Measuring the misfit between seismograms using an optimal transport distance: application to full waveform inversion. *Geophysical Journal International* 205, 345–377. <https://doi.org/10.1093/gji/ggw014>
- Morgan, J., Warner, M., Bell, R., Ashley, J., Barnes, D., Little, R., Roele, K., Jones, C., 2013. Next-generation seismic experiments: wide-angle, multi-azimuth, three-dimensional, full-waveform inversion. *Geophysical Journal International* 195, 1657–1678. <https://doi.org/10.1093/gji/ggt345>
- Musayev, K., Lamert, A., Hackl, K., Friederich, W., Baitsch, M., 2016. Predicting the geological structure ahead of a tunnel using full waveform inversion - a blind test. Presented at the 78th EAGE Conference and Exhibition 2016, European Association of Geoscientists & Engineers, pp. 1–5. <https://doi.org/10.3997/2214-4609.201600793>
- Nguyen, L.T., Nestorović, T., 2018. Reconstructing disturbance zones ahead of the tunnel face by elastic waveform inversion supported by a parametric level-set representation. *Soil Dynamics and Earthquake Engineering* 115, 606–621. <https://doi.org/10.1016/j.soildyn.2018.09.025>
- Ovcharenko, O., Kazei, V., Kalita, M., Peter, D., Alkhalifah, T., 2019. Deep learning for low-frequency extrapolation from multioffset seismic data. *Geophysics* 84, R989–R1001. <https://doi.org/10.1190/geo2018-0884.1>
- Petronio, L., Poletto, F., Schleifer, A., 2007. Interface prediction ahead of the excavation front by the tunnel-seismic-while-drilling (TSWD) method. *Geophysics* 72, G39–G44. <https://doi.org/10.1190/1.2740712>
- Qi, L., Jiang, H., 1997. Semismooth karush-kuhn-tucker equations and convergence analysis of newton and quasi-newton methods for solving these equations. *Mathematics of OR* 22, 301–325. <https://doi.org/10.1287/moor.22.2.301>
- Riedel, C., Musayev, K., Baitsch, M., Hackl, K., 2023. Elastic waveform inversion in the frequency domain for an application in mechanized tunneling. *Tunnelling and Underground Space Technology* 137, 105114. <https://doi.org/10.1016/j.tust.2023.105114>
- Riedel, C., Musayev, K., Baitsch, M., Zhu, H., Hackl, K., 2021. Acoustic waveform inversion in frequency domain: application to a tunnel environment. *Underground Space* 6, 560–576. <https://doi.org/10.1016/j.undsp.2021.01.001>
- Sun, L., Fang, C., Sa, L., Yang, P., Sun, Z., 2015. Innovation and prospect of geophysical technology in the exploration of deep oil and gas. *Petroleum Exploration and Development* 42, 454–465. [https://doi.org/10.1016/S1876-3804\(15\)30038-0](https://doi.org/10.1016/S1876-3804(15)30038-0)
- Takekawa, J., Mikada, H., 2018. A mesh-free finite-difference method for elastic wave propagation in the frequency-domain. *Computers & Geosciences* 118, 65–78. <https://doi.org/10.1016/j.cageo.2018.05.011>
- Takekawa, J., Mikada, H., 2016. An absorbing boundary condition for acoustic-wave propagation using a mesh-free method. *Geophysics* 81, T145–T154. <https://doi.org/10.1190/geo2015-0315.1>
- Tarantola, A., 1984. Inversion of seismic reflection data in the acoustic approximation. *Geophysics* 49, 1259–1266. <https://doi.org/10.1190/1.1441754>

- Trapp, M., Nestorović, T., 2022. Non-gradient full waveform inversion approaches for exploration during mechanized tunneling applied to surrogate laboratory measurements. *Tunnelling and Underground Space Technology* 120, 104252. <https://doi.org/10.1016/j.tust.2021.104252>
- Tromp, J., 2020. Seismic wavefield imaging of earth's interior across scales. *Nat Rev Earth Environ* 1, 40–53. <https://doi.org/10.1038/s43017-019-0003-8>
- van Leeuwen, T., Herrmann, F.J., 2013. Mitigating local minima in full-waveform inversion by expanding the search space. *Geophysical Journal International* 195, 661–667. <https://doi.org/10.1093/gji/ggt258>
- Virieux, J., Operto, S., 2009. An overview of full-waveform inversion in exploration geophysics. *Geophysics* 74, WCC1–WCC26. <https://doi.org/10.1190/1.3238367>
- Wai-Lok Lai, W., Dérobert, X., Annan, P., 2018. A review of ground penetrating radar application in civil engineering: a 30-year journey from locating and testing to imaging and diagnosis. *NDT & E International* 96, 58–78. <https://doi.org/10.1016/j.ndteint.2017.04.002>
- Wang, X., Feng, D., 2021. Multiparameter full-waveform inversion of 3-D on-ground GPR with a modified total variation regularization scheme. *Ieee Geoscience and Remote Sensing Letters* 18, 466–470. <https://doi.org/10.1109/LGRS.2020.2976146>
- Xu, Z., Liu, F., Lin, P., Shao, R., Shi, X., 2021. Non-destructive, in-situ, fast identification of adverse geology in tunnels based on anomalies analysis of element content. *Tunnelling and Underground Space Technology* 118, 104146. <https://doi.org/10.1016/j.tust.2021.104146>
- Yu, M., Cheng, F., Liu, J., Peng, D., Tian, Z., 2022. Frequency-domain full-waveform inversion based on tunnel space seismic data. *Engineering* 18, 197–206. <https://doi.org/10.1016/j.eng.2021.06.018>
- Zhang, N., Shen, J.S., Zhou, A., Arulrajah, A., 2018. Tunneling induced geohazards in mylonitic rock faults with rich groundwater: a case study in guangzhou. *Tunnelling and Underground Space Technology* 74, 262–272. <https://doi.org/10.1016/j.tust.2017.12.021>



## Figure Captions

**Fig. 1.** Visualization and simulation of the  $W_p^1$  regularization. (a)  $p$  values ranging from 0.5 to 2, the azimuth angle (az) is 50, and the elevation angle (el) is 15, (az: 50, el: 15). (b)  $p$  values ranging from 0.5 to 2, the az is negative 50, the elevation angle (el) is 15, (az: -50, el: 15). (c)  $p$  values ranging from 0.5 to 0.7, which exhibits the characteristics of the 0.5 norm. (d)  $p$  values ranging from 1 to 1.2, which exhibits the characteristics of TV regularization. (e)  $p$  values ranging from 1.5 to 1.7, which exhibits the characteristics of the 1.5 norm. (f)  $p$  value is equal to 2, which exhibits the characteristics of the Tikhonov regularization.

**Fig. 2.** Schematic of the model structure. (a) Tunnel structural model with an inclined fault. (b) The modelling results after tilting the schematic **Fig. 2(a)**, the top of the modelling is a free surface to simulate the real ground surface (the number of receivers in the schematic does not represent the real number of receivers).

**Fig. 3.** Modelling of a fault structure for tunnel advance prediction. (a) Benchmark of the model with a tilted fault. (b) The initial model of the benchmark. The tunnel structure was removed for inversion self-consistency testing.

**Fig. 4.** Forward wavefield information. (a) The real part of the forward wavefields. (b) The imaginary part of the forward wavefields. (c) The real part of the initial background wavefield. (d) The imaginary part of the background wavefield.

**Fig. 5.** Source receiver wavefield for the tunnel model. (a) The real part of the clean wavefield without noise component. The vertical coordinate explicit acquisition system consists of two seismic sources, horizontal coordinates from 1 to 26 for receivers on the free surface and from 27 to 33 for receivers on the tunnel floor. (b) The imaginary part of the clean wavefield without noise component. (c) The real part of the random noise. (d) The imaginary part of the random noise. (e) The real part of the wavefield with random noise as a means for further inversion. (f) The imaginary part of the wavefield with random noise as a means for further inversion.

**Fig. 6.** Comparison of inversion tests with different scaling factors  $\gamma$  for maximum eigenvalues  $\mathbf{A}^{-T}\mathbf{P}^T\mathbf{P}\mathbf{A}^{-1}$ . (a)  $\gamma = 1e-2$ . (b)  $\gamma = 1e-1$ . (c)  $\gamma = 1e0$ . (d)  $\gamma = 1e2$ . In the inversion results, the black dashed line represents the specific locations of a set of velocity contrasts we sampled. Directly below the inversion results, a set of vertical velocity contrasts is displayed, where the black solid line corresponds to the benchmark velocity, the red solid line to the inverted velocity, and the grey dashed line to the initial velocity. As the scaling factor increases, leading to a smaller reciprocal of the scaling factor, the inversion results tend to become unstable due to the dominance of the data mismatch term. Conversely, with smaller scaling factors, resulting in a larger reciprocal of the scaling factor, the inversion results are more stable as the wave equation term becomes more predominant.

**Fig. 7.** Maximum eigenvalue curve of  $\mathbf{A}^{-T}\mathbf{P}^T\mathbf{P}\mathbf{A}^{-1}$  in relation to the penalty parameter  $\tau$  in Eq. (8). The curves are shown for three different scaling levels,  $\gamma = 1e-2$  in red,  $\gamma = 1e-1$  in green,  $\gamma = 1e0$  in blue and  $\gamma = 1e2$  in magenta.

**Fig. 8.** Relative importance of the data mismatch term and the wave equation penalty term in the initial stage of the inversion. The curves are shown for four different scaling levels,  $\gamma = 1e-2$  in red,  $\gamma = 1e-1$  in green,  $\gamma = 1e0$  in blue and  $\gamma = 1e2$  in magenta. Smaller scaling factors can ensure that both terms maintain convergent behaviour simultaneously. At  $\gamma = 1e-2$ , the data mismatch term declines rapidly, but the wave equation term does not reduce to the same level as the data mismatch term, suggesting the possibility of the wave equation term falling into a local minimum. At  $\gamma = 1e-1$ , the wave equation term converges slightly faster than the data term, and both decline synchronously. At  $\gamma = 1e0$ , the two terms maintain nearly identical speeds. However, at  $\gamma = 1e2$ , the wavefield term's correlation with the data mismatch term is too small, potentially leading to a scenario where the data term converges independently. Importantly, at this scaling, the data mismatch term does not reduce to a level nearly similar to that of the wave equation term and declines noticeably slower, indicating that the data mismatch term has fallen into a local minimum.

**Fig. 9.** Sensitivity analysis of different parameters  $\tau$ . (a) Convergence process of the data mismatch penalty term of the objective function. (b) Convergence process of the wave equation penalty term of the objective function. Construction of the objective function according to Eq. (5). The curves are shown for four different scaling levels,  $\gamma = 1e-2$  in red,  $\gamma = 1e-1$  in green,  $\gamma = 1e0$  in blue and  $\gamma = 1e2$  in magenta. Additionally, the larger the regularization parameter, the more pronounced the loss spike phenomenon becomes. For the specific model discussed, iterations fewer than 100 are sufficient. Excessive iterations have resulted in a very slight degree of overfitting.

**Fig. 10.** Inversion results comparison. (a1)-(a7) Tikhonov - FWI regularization at 3.0 Hz, 3.6 Hz, 4.0 Hz, 4.8 Hz, 5.8 Hz, 6.4 Hz and 7.1 Hz. (b1)-(b7) TV - FWI in the same frequency range. (c1)-(c7) Proposed method in the same frequency range and  $\gamma = 1e-2$ . (d1)-(d7) Proposed method in the same frequency range but  $\gamma = 1e-1$  case. The green polygons identify the areas of low-velocity artefacts. Horizontal (a8)-(d8) are direct copies from (a7)-(d7). The black dashed lines indicate the target locations for subsequent velocity profile analyses. V-1 and V-2 represent two sets of vertical sample traces located at 150 m and 170 m, respectively, while H-1 and H-2 represent two sets of horizontal sample traces located at 52 m and 65 m, respectively.

**Fig. 11.** The final residual gradient of the inversion. (a) FWI based on the Tikhonov regularization. (b) FWI based on TV regularization. (c) FWI based on the proposed method and  $\gamma = 1e-2$ . (d) FWI based on the proposed method but  $\gamma = 1e-1$  case. The gradients of Fig. 11(b) and others vary by one order of magnitude, with the minimum and maximum gradient ranging from Fig. 11(b) at  $[-5e-4, 5e-4]$  and that of others at  $[-5e-5, 5e-5]$ .

**Fig. 12.** Model increments at the 30th iteration. (a) Tikhonov regularization. (b) TV regularization. (c) Proposed modified FWI and  $\gamma = 1e-2$ . (d) Proposed modified FWI but  $\gamma = 1e-1$ .

**Fig. 13.** Horizontal velocity profile analysis. (a) 52 m. (b) 65 m. The grey dotted line represents the initial velocity. The black dashed line represents the velocity of the benchmark; the magenta solid line represents the Tikhonov

regularization FWI; the blue solid line represents the TV regularization FWI; the red solid line denotes the  $\gamma = 1e-2$  proposed modified FWI results velocity profile; the green solid line denotes the  $\gamma = 1e-1$  proposed modified FWI results velocity profile. The closer it approaches the black dashed line, the better the inversion results.

**Fig. 14.** Vertical velocity profile analysis. (a) 150 m. (b) 170 m. The grey dotted line represents the initial velocity. The black dashed line represents the velocity of the benchmark; the magenta solid line represents the Tikhonov regularization FWI; the blue solid line represents the TV regularization FWI; the red solid line denotes the  $\gamma = 1e-2$  proposed modified FWI results velocity profile; the green solid line denotes the  $\gamma = 1e-1$  proposed modified FWI results velocity profile. The closer it approaches the black dashed line, the better the inversion results.

**Fig. 15.** Modelling of a dual faults structure for tunnel advance prediction. (a) Benchmark of the model with two tilted faults. (b) The initial model of the benchmark. The grey dotted lines indicate the location of the faults. All two faults have a width of 5 m.

**Fig. 16.** Source receiver wavefield for the dual faults tunnel model. (a) The real part of the clean wavefield without noise component. The vertical coordinate explicit acquisition system consists of ten seismic sources, horizontal coordinates from 1 to 7 for receivers on the tunnel floor and from 8 to 32 for receivers on the free surface. (b) The real part of the random noise. (c) The real part of the wavefield with random noise as a means for further inversion.

**Fig. 17.** The forward and background wavefields; and the scattered wavefields after the 1st iteration. (a1)-(a2) The real and imaginary part of the forward wavefield at 3.0 Hz. (b1)-(b2) The real and imaginary part of the background wavefield at 3.0 Hz. (c1)-(c2) The real and imaginary part of the scattered wavefield of LS method-based FWI at 3.0 Hz. (d1)-(d2) The real and imaginary part of the scattered wavefield of the quadratic penalty method-based FWI and  $\gamma = 1e-1$  at 3.0 Hz. The position of the grey auxiliary lines correspond to that in the true model.

**Fig. 18.** Data for the 5th source and the 1st iteration. (a) The real part of the data received by receivers No.1-7. (b) The real part of the data received by receivers No.8-32. (c) The imaginary part of the data received by receivers No.1-7. (d) The imaginary part of the data received by receivers No.8-32. Since the LS simulated data has a significant shift from the observed data, we consider its inversion to be difficult.

**Fig. 19.** Inversion results comparison. (a1)-(a3) Tikhonov-FWI regularization at 2.0 Hz, 3.5 Hz and 7.5 Hz. (b1)-(b3) TV-FWI in the same frequency range. (c1)-(c3) Proposed method in the same frequency range and  $\gamma = 1e-1$ . The position of the grey auxiliary lines correspond to that in the true model.

**Fig. 20.** A 20 m wide dual faults model. (a) True model (b) Initial model. (c) Forward wavefield at 1 Hz. (d) Forward wavefield at 2 Hz. (e) Forward wavefield at 3 Hz. The position of the coloured auxiliary lines correspond to that in the true model.

**Fig. 21.** Inversion results comparison. (a)-(d) Tikhonov-FWI regularization at 1.0 Hz, 2.0 Hz, 3.0 Hz and 4.0 Hz. (e)-(h) Proposed method in the same frequency range and  $\gamma = 1e-1$ . The position of the coloured auxiliary lines correspond to that in the true model.